Uniaxial tensile behavior of ultra-high performance fiber-reinforced concrete (uhpfrc): Experiments and modeling

UNIAXIAL TENSILE BEHAVIOR OF ULTRA-HIGH PERFORMANCE FIBER-REINFORCED CONCRETE (UHPFRC): EXPERIMENTS AND MODELING

Jacopo Donnini[1], Giovanni Lancioni[2*], Gianluca Chiappini[3], Valeria Corinaldesi[4]

[1] Department of Materials, Environmental Sciences and Urban Planning (SIMAU), Polytechnic University of Marche, via Brecce Bianche, Ancona, Italy, jacopo.donnini@staff.univpm.it

[2] Department of Civil and Building Engineering and Architecture (DICEA), Polytechnic University of Marche, via Brecce Bianche, Ancona, Italy, g.lancioni@staff.univpm.it

[3] eCampus telematic University, Via Isimbardi 10, Novedrate (CO), Italy, g.chiappini@univpm.it

[4] Department of Materials, Environmental Sciences and Urban Planning (SIMAU), Polytechnic University of Marche, via Brecce Bianche, Ancona, Italy, v.corinaldesi@staff.univpm.it

[*] Corresponding auhor

HIGHLIGHTS

- Uniaxial tensile tests on UHPFRC dog-bone shaped specimens;
- Influence of different fiber dosages on mechanical properties;
- Use of Digital Image Correlation (DIC) to monitor displacements and strains during the experimental tests;
- Phase-field model which schematizes UHPFRC as a mixture of brittle and elasto-plastic phases, accounting for concrete matrix and fiber reinforcement, respectively.
- FE numerical implementation of the variational model and simulations to reproduce different failure processes.

ABSTRACT

Ultra-High Performance Fiber-Reinforced Concrete (UHPFRC) is considered a promising material for many structural applications where high strength and high energy absorption capacity are required.
The purpose of this work is to study the uniaxial tensile behavior of soft cast (flowable at casting time) UHPFRC by varying the amount of hooked steel fibers (30-mm long) from 0% up to 2.55% by volume. Direct tensile tests have been performed on dog-bone shaped specimens and Digital Image Correlation (DIC) has been used to measure displacements and deformations and to monitor the evolution of cracks. Then, a phase-field model has been implemented in a FE code and numerical simulations have been performed to better understand the effects of different fiber dosages on the mechanical behavior of UHPFRC composites and on their post-elastic evolution. Concrete matrix and fiber reinforcement have been modeled as brittle and elasto-plastic phases of a mixture, whose internal energies are enriched by non-local damage and plasticity contributions. The different failure mechanisms observed in experiments have been reproduced, including the ductile failure experienced by specimens with sufficiently high fiber dosage, which distinguishes for a strain-hardening phase of matrix multi- micro-cracking that anticipates material failure.

Keywords:

UHPFRC; steel fibers; tensile tests; Digital Image Correlation; phase-field modeling; damage and plasticity.

1. Introduction

The interest of the scientific community on the development of Ultra-High Performance Fiber-Reinforced Concrete (UHPFRC) is significantly increased in recent years. UHPFRC is a composite cement-based material, usually reinforced with short steel fibers, characterized by high compressive strength (>120 MPa) [1,2]. Furthermore, UHPFRC exhibits high tensile strength, exceptional energy absorption before failure (toughness) and pseudo-ductility in tension, with the formation of distributed small cracks prior to crack localization [3–5]. Thanks to its great mechanical properties, this material can be used to realize building components (reducing the weight by more than 50% compared to ordinary concrete structures under the same loading conditions), architectural features, off-shore and hydraulic structures, impacts or explosions resistant elements or even as external reinforcement for existing concrete structures [6–9].

To achieve ultra-high compressive strength, in addition to a high amount of cement and a low water-to-cement ratio (usually ≤ 0.2), fine powders such as quartz flour, ground granulated blast-furnace slag and silica fume are normally added to the mixture to ensure a highly dense matrix [10–16].

Studies from the literature have clearly demonstrated that the addition of fibers reduces the brittle behavior of plain concrete under tensile and bending loading and allows the material to increase its ultimate tensile strain capacity and ductility [10,17,18]. However, a cementitious material with deflection-hardening post-cracking behavior in bending tests does not necessarily show a strain-hardening behavior in uniaxial tensile tests [19,20]. To fulfill the second goal the UHPFRC matrix must have a fiber content exceeding a certain threshold (>1.5% by volume) [21]. Mechanically deformed fibers may improve the bond with the matrix and enhance the material ductility [20]. UHPFRC properties can be improved to such a point that, when the specimen is subjected to uniaxial tensile stress, it may exhibit multiple fine cracks and strain-hardening behavior in the post-cracking phase. This phenomenon, observed by some researchers [19–21], is generally accompanied by the formation of multiple transversal cracks at different specimen cross-sections. Tensile strength and post-cracking deformation capacity of UHPFRC can be evaluated through uniaxial direct tensile tests. The advantage of using this type of test, despite some complexities in the execution, is the capability to directly investigate the material tensile behavior over all the three main stages that are usually observed: linear elastic, strain-hardening, associated to micro- and multi-cracking within the matrix, and strain-softening, related to the development of macro-cracks [21]. The strain-hardening stage is due to the stress bridging action of fibers among cracks, and it confers enhanced ductility to the composite.

Some recommendations on how to perform direct tensile tests on UHPFRC materials have been provided by few national guidelines, such as the French AFGC-SETRA [1] and the Japanese JSCE [2]. The Fib Model Code 2010 [22], which serves as a basis for future code for concrete structures, gives important information on the mechanical properties of Fiber Reinforced Concrete (FRC) elements. However, it does not provide instructions on how to perform direct tensile tests. Some indications on fiber reinforced concrete (with no references to UHPFRC) are provided by the Italian guidelines issued by CSLLPP [23] and CNR [24].

Different tensile test setups have been proposed in order to obtain reliable results [8,21,25,26], since there are still no standardized testing procedures to fully characterize the tensile properties of UHPFRC. Furthermore, specimen's geometry (dog-bone shape, unnotched and notched prisms

or cylinders) and dimensions, together with the gripping method used during the test (fixed or rotating boundary condition), can significantly influence the experimental results [21]. Notched specimens, for example, are not suitable for characterizing cementitious materials with strain-hardening tensile behavior due to stress localization and earlier crack initiation.
Strain-hardening behavior can be successfully captured by using dog-bone shaped specimens, having a central part with constant cross-sectional area and larger areas at the specimen ends to avoid support failure. Tensile tests on dog-bone shaped specimens with different dimensions and different grip systems have been performed [16,20,21,25–31]. Wille et al. [21] experimentally investigated the direct tensile behavior of nine dog-bone shaped UHPFRC specimens, by varying the fiber type and the fiber volume fraction. The analyzed results showed a strong dependency on the fiber volume fraction. In Yoo D. et al. [31], the effects of different steel fibers on the tensile performance of UHPFRC were investigated. Four different steel fiber types were used: S-straight, T-twisted, H-hooked, and HH-half-hooked. The order of effectiveness in enhancing the tensile performance of dog-bone specimens was S-fiber, T-fiber, HH-fiber and H-fiber. Hassan et al. [16] carried out direct tensile tests on two types of dog-bone shaped specimens with different geometries. Specimens were glued with epoxy on two metal plates and strains were measured using two LVDTs. Specimens geometry appeared to have no influence on the tensile strength of UHPFRC. Jun and Mechtcherine [26] carried out tensile tests on dumbbell shaped prisms of strain-hardening cement based composites (SHCC) by using non-rotatable boundary conditions and measuring deformations by means of two LVDTs fixed to the specimen lateral surfaces.

In this study, the uniaxial tensile behavior of different UHPFRC mixtures has been investigated, by varying the amount of hooked steel fibers (30 mm length) from 0.6% up to 2.55% by volume. The UHPFRC matrices studied herein are easily reproducible on site, therefore they can be produced with standard tools and without the need for special equipment. Before testing, specimens were cured at laboratory conditions (20 °C, 70% RH) up to 28 days, which correspond to the simplest way of producing soft cast UHPFRC [32] and could represent the real conditions on site.
Uniaxial tensile tests have been performed on unnotched dog-bone shaped specimens (length of 330 mm and cross-sectional area of 45x30 mm^2) by using a test setup which allows rotation of the specimen around one axis. Digital Image Correlation (DIC) has been used to measure displacements and strains and to monitor the formation of cracks and the damage evolution during tensile tests.
Experimental results have been supported by a modelling study, aimed at a comprehensive understanding of the influence of steel fiber amount on the tensile properties of UHPFRC and on its failure mechanisms. The UHPFRC tensile behavior has been modeled by using the phase-field model proposed in [33]. The model assumes that the composite is a mixture of two material phases, the cementitious matrix and the reinforcing fibers. Concrete and reinforcement phases are supposed to be brittle and elasto-plastic, respectively, and their internal energies are enriched by damage and plastic contributions. The damage energy assigned to the brittle matrix depends on a scalar damage parameter, and it is sum of a local and a non-local term, as typically considered in phase-field models of fracture [34]. The plastic energy of the reinforcement is similar to that proposed in [35–37], and it is constituted by a local non-convex term, which depends on the cumulated plastic strain, having a dissipative nature, and a non-local term, depending on the gradient of the cumulated plastic strain, and playing the role of strain localization limiter [38].
While damage and plasticity are combined within the same material in [39,40], in the present model they are assigned separately to each component of the mixture. The two material phases are linked through linear elastic bonds, which contribute to couple damage and plastic problems associated to each phase. The model provides an accurate description of the micro- multi-cracking

process observed in UHPFRC with high fiber content, significantly improving the description given by the damage model [41], where multiple cracks were undistinguished, spread within zones of diffused damage.
A key assumption of the proposed model is that damage and plastic properties of the two phases account for all inelastic phenomena observed in experiments. Indeed, damage properties of matrix allow to describe micro- and multi-cracking. Plastic properties of reinforcement account for the plastic stretching of fibers and, mostly, for all inelastic phenomena that occur at the interface level in real UHPFRCs, such as fiber-aggregate interlocking and matrix-fibers frictional mechanisms. Finally, matrix to fibers interface bonds have just the role of transferring stresses between the two phases. They have been modeled by linearly elastic springs, since non-linearities related to debonding and sliding are included into the plastic energy of the reinforcement phase. These simplistic assumptions make the model phenomenological in nature, and, thus, not related to any micro-mechanical justification. The advantage of this framework is that the effects of each modelling ingredient are clearly recognized in the description of the failure process. Consequently, the model constitutive parameters can be easily calibrated, by associating each of them to a single mechanical phenomenon that can be observed and measured in experiments.
Damage, plastic and bond energies incorporates three different internal lengths, which are the size of micro-crack process zone, the size of final macro-crack process zone, and the spacing between adjacent micro-cracks, which represent crucial parameters in the description of the inelastic evolution process of multiple cracking.
The variational model is implemented in a FE code, and numerical simulations are performed to reproduce tensile tests. Experimental stress-strain curves have been accurately reproduced, as well as the different stages of the cracking processes that lead samples to failure. Furthermore, numerical simulations have given valuable insights into the influence of fibers amount on the transition from brittle to ductile failure in the UHPFRC uniaxial tensile behavior.

The paper is organized as follows. In Sect. 2, the materials and mixture proportions of UHPFRC are described, and the samples casting and curing process are outlined. The influence of the casting process on the distribution of fibers within the samples is investigated in Subsect. 2.3. The experimental set-up of direct tensile tests, the DIC acquisition system technique and the main results are presented in Sect. 3. The variational model is described in Sect. 4, where the theory is formulated in the one-dimensional format since, despite its simplicity, it preserves the key modelling features, and provides formulas for parameters calibration. The general three-dimensional problem is provided in Subsects. 4.3 and 4.4. Numerical results and comparisons with experiments are presented in Sect. 5. The two different quasi-brittle and ductile behavior in the cracking evolution process, associated to UHPFRC with different fibers content, are discussed. Finally, conclusions are drawn in Sect. 6.

2. Materials and methods

2.1 Materials and mixture proportions

A Commercial Portland-limestone blended cement CEM I 52.5 R, in compliance with EN-197/1 was used [42]. The Blaine fineness of cement was 0.48 m^2/g and its relative specific gravity was 3.15. As aggregate, two different types of quartz micro-sand with particle size 0-0.6 mm and 0.6-1.0 mm were suitably combined. Silica fume was added at dosage of 125 kg/m^3. In addition, an acrylic-based water-reducing admixture (WRA) was added in powder at dosage of 1.1% by weight of cement, and a water to cement ratio (w/c) of 0.20 was adopted in all mixtures.

Hooked steel fibers (showed in Fig. 1), 30-mm long with aspect ratio equal to 43, were added at increasing dosages: 50, 100, 150 and 200 kg/m^3. The corresponding fibers volume fractions are 0.6%, 1.25%, 1.9% and 2.55%. The mixture proportions are shown in Table 1, while the main characteristics of steel fibers, as reported by manufacturer, are listed in Table 2.
The concrete mixture without fibers (UHPC) was cast into three prismatic specimens having dimensions of 40x40x160 mm^3. After 2 days specimens were demolded and cured up to 28 days at laboratory conditions (20°C, 70% R.H.) before testing in bending and compression, according to the procedure described in EN 1015-11 [43]. Results obtained are listed in Table 3.

Figure 1. Hooked steel fibers and dog-bone shaped specimens manufacturing.

Table 1. UHPFRC mixtures proportions by weight.

Mixture	CEM I 52.5R	Water	Sand 0/0.6	Sand 0.6/1.0	Silica fume	WRA	Fibers
UHPC_0%	1	0.2	0.4	0.6	0.125	0.011	-
UHPFRC_0.6%	1	0.2	0.4	0.6	0.125	0.011	0.05
UHPFRC_1.25%	1	0.2	0.4	0.6	0.125	0.011	0.10
UHPFRC_1.9%	1	0.2	0.4	0.6	0.125	0.011	0.15
UHPFRC_2.55%	1	0.2	0.4	0.6	0.125	0.011	0.20

Table 2. Main characteristics of the steel fibers used.

	Length (mm)	Diameter (mm)	Aspect ratio	Young modulus (GPa)	Tensile strength (MPa)
Hooked steel fiber	30	0.7	43	170	450

Table 3. Mechanical properties of the UHPC reference mixture (CoV in round brackets).

Specimen	Compressive strength (MPa)	Flexural strength (MPa)
UHPC_0%	122.5 *(5%)*	15.8 *(5%)*

2.2 Dog-bone shaped specimens for uniaxial tensile tests

Uniaxial tensile tests have been carried out on dog-bone shaped specimens with nominal cross-sectional area of 30x45 mm^2 and total length of 330 mm (Fig. 2). The dimensions of the specimen cross-section have been defined in order to minimize the alignment effect along the longitudinal direction and, at the same time, minimize the bending stresses and the eccentricity that could arise during tensile tests for specimens with too large sections.
Specimens were cast in wood frameworks (Fig. 1) and after 2 days demolded and cured at laboratory conditions (20 °C, 70% R.H.) up to 28 days before testing.

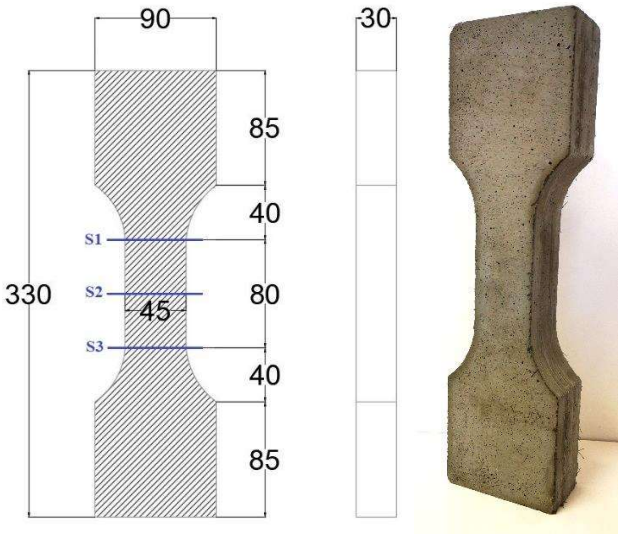

Figure 2. UHPFRC dog-bone shaped specimens.

2.3 Fibers distribution analysis

Fibers dispersion and distribution within the concrete specimen can significantly affect the mechanical behavior of the material [44,45]. In fact, while the fibers alignment along one axis of the specimen could be favorable for an element subjected to uniaxial or flexural stress in that direction, randomly oriented fibers would be required for such applications where multiaxial stress states are present. In this study, the fibers distribution within the specimen cross-section has been evaluated through image analysis.
One dog-bone shaped specimen for each group has been cut at three different sections (indicated as S1, S2, S3 in Fig. 2), perpendicular to the main axis of the specimen, in order to check the fibers distribution at different specimen cross-sections.
Pictures of the specimen cross-sections have been acquired using grazing light illumination in such a way that the steel fibers, being reflective, were more evident in the image (see Table 4).
The acquired pictures were converted into binary image by using a picture processing software developed with Matlab. The area A_{sec} in pixels of each specimen section has been identified. White pixels (A_w) represent the sectional area occupied by steel fibers, therefore, the percentage of fibers area within each section (A_f) can be calculated as:

$$A_f = \frac{A_w}{A_{sec}}$$

The average fibers area evaluated on three sections for each specimen has been reported as $A_{f,AVG}$ in Table 4. Then, the ratio between $A_{f,AVG}$ and the nominal fibers volume within the mixture (V_f) has been reported in the last column of Table 4.

From the cross-section pictures of Table 4 some fibers segregation can be observed in specimens with low fibers content (UHPFRC_0.6% and UHPFRC_1.25%). The inhomogeneous fibers distribution was probably due to the dosage of WRA, which has been kept constant in all mixtures, thus producing too fluid matrices when a low percentage of fibers has been used. On the other hand, when a higher fibers dosage was adopted (UHPFRC_1.9% and UHPFRC_2.55%) a more homogeneous fibers distribution has been noticed. Despite the fact that some variability has been observed in the fibers distribution at the three cross-sections analyzed for each specimen (see Coefficients of Variation (%) reported in Table 4), it is interesting to observe that the rate between the average fibers area within the cross section ($A_{f,AVG}$) and the nominal fibers volume within the mixture (V_f) is almost constant for all the mixtures, and equal to values comprised between 1.7 and 1.9.

Table 4. Fibers distribution within the dog-bone shaped specimen cross-sections.

Specimen	Cross-sections of dog-bone shaped specimens	Nominal fibers volume within the mixture, V_f (% vol)	Fibers area measured at different cross-sections (% area)	Average fibers area within the cross section, $A_{f,AVG}$ (% area)	$A_{f,AVG}/V_f$
UHPFRC_0.6%	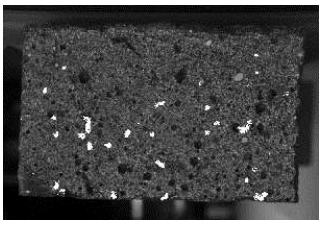	0.6	S1 = 1.08 S2 = 1.06 S3 = 1.10	1.08 CoV = 1.9%	1.80
UHPFRC_1.25%	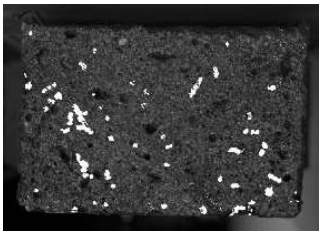	1.25	S1 = 1.89 S2 = 3.00 S3 = 2.20	2.36 CoV = 24.2%	1.89
UHPFRC_1.9%	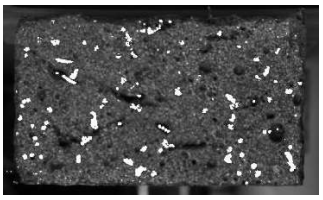	1.9	S1 = 3.83 S2 = 3.52 S3 = 2.49	3.28 CoV = 21.4%	1.73
UHPFRC_2.55%	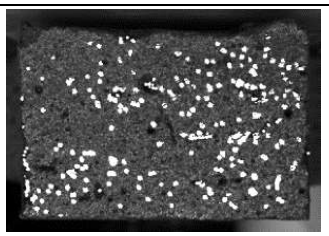	2.55	S1 = 3.79 S2 = 3.79 S3 = 5.45	4.34 CoV = 22.1%	1.70

3. Direct tensile tests on dog-bone shaped specimens

3.1 Test setup

A steel frame realized with welded steel plates and four steel cylinders (Fig. 3) was used to grab the specimen and to transfer the tensile force without applying compression at the specimen ends and allowing rotations around one axis. Tensile tests were performed in displacement control (loading rate of 0.5 mm/min) with a tensile testing machine having a load capacity of 50 kN. Tensile stress σ was calculated by dividing the tensile load by the specimen's cross section. Digital Image Correlation (DIC) was used to monitor strains and displacements on a selected area of the sample (the red area in Figure 3). More information on the DIC technique used in this study and on the test apparatus are provided in the next section.

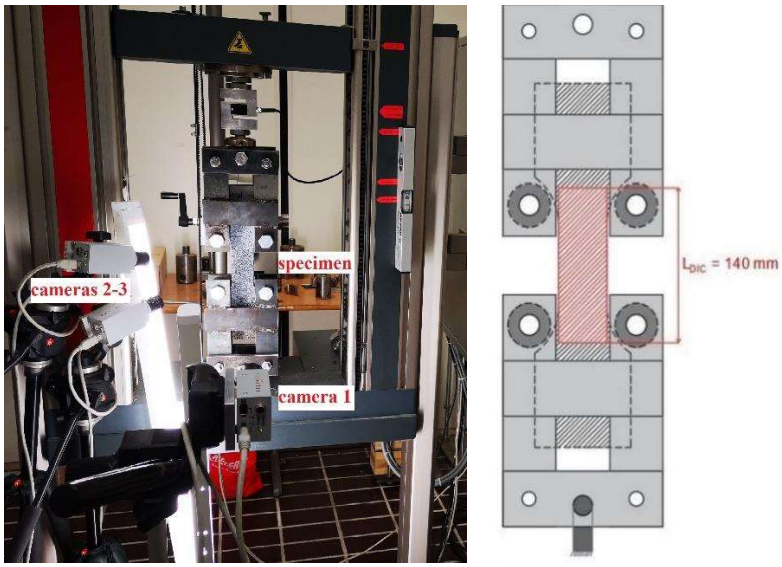

Figure 3. Direct tensile test setup and DIC acquisition area.

3.2 Digital Image Correlation (DIC) acquisition system

The measurement of displacements and deformations of UHPFRC specimens during tensile tests was performed by using optical methods. In order to perform the Digital Image Correlation (DIC) analysis, three digital cameras (model Pixelink® B371F) have been used to acquire pictures of the frontal and lateral surfaces of the samples during all tests.
Figure 3 shows the measurement setup used: the camera 1, equipped with a lens having a focal length of 25 mm and placed about 600 mm away from the specimen, was used to acquire the whole frontal surface and the acquired images were then used to apply 2D-DIC measurements.
Cameras 2 and 3, equipped with a lens having a focal length of 12 mm and placed about 200 mm from the sample, have been used to acquire the lateral and frontal surface in the central area of the specimens, in order to apply stereo-3D-DIC measurements.
The specimen surfaces were properly prepared with a b/w speckle pattern for the subsequent DIC analysis and illuminated using a neon spotlight during tensile tests. The size of the spots was chosen in relation to the size of the specimens and the position of the cameras.

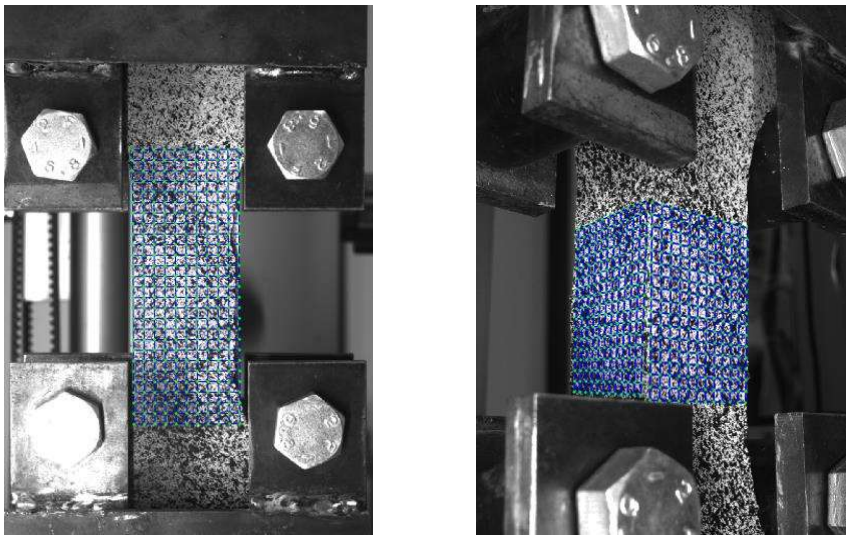

(a) (b)

Figure 4. Speckled surfaces with superimposed DIC subsets grid in 2D-DIC (a) and stereo-3D-DIC (b) test samples.

An example of images of the speckled samples, with superimposed the virtual grid used in the DIC analysis, is given in Fig. 4 for frontal and lateral cameras.

The pictures acquired during the tests have been post-processed by an in-house developed DIC software. The correlation method is based on the global DIC approach [46], and, for stereo-3D, incorporates the epipolar constraint and the assembling approach of Finite Element Method.

The random error, principally due to gray level noise, was evaluated by processing a sequence of images of the fixed samples; the RMS of the random error was 40 με for the 2D-DIC set-up, while it increased to 70 με for the stereo-3D-DIC.

Displacements of all nodes of the grid, with subset size of 24×24 and 28×28 pixel for the 2D-DIC and stereo-3D-DIC setups, respectively, are obtained by minimizing the correlation error computed all over the current frame with respect to the reference frame [46]. The zero-mean sum of square difference (ZSSD) criterion was adopted to avoid the effects of lighting offset and inhomogeneity.

The strain maps have been computed by means of the Cauchy-Green theory, within the framework of large displacements and large deformations, starting from the node displacements. The components of the Hencky strain tensor ε_x, ε_y, and ε_{xy} have been computed.

The stereo-3D-DIC measurements were used to calculate any possible out-of-plane displacement of the specimens during the test, due to the particular setup used to grip the specimens. The out-of-plane displacements thus obtained were used to correct the strain measured by the frontal camera with the 2D-DIC technique, according to [47,48].

Strains reported in Table 5 ($\varepsilon_{t,c}$, $\varepsilon_{t,max}$), and those of the experimental curves of Fig. 5, were calculated by using the 2D-DIC technique. Global strain was calculated by measuring the mean strain over a length equal to 140 mm (Fig. 3), in order to include all the cracks found during the tensile test. A sequence of axial displacement and strain maps, measured at different instants, is reported in next section (Fig.6).

3.3 Tensile test results

Results of direct tensile tests in terms of tensile stress at first cracking $\sigma_{t,c}$, maximum tensile stress $\sigma_{t,max}$, axial strain at first crack $\varepsilon_{t,c}$ and strain at maximum tensile stress $\varepsilon_{t,max}$ have been reported in Table 5 as average values of 3 specimens for each group, with corresponding Coefficient of Variation (%) in round brackets.

Table 5. Experimental results of direct tensile tests on dog-bone shaped specimens (CoV in round brackets).

Specimen	$\sigma_{t,c}$ (MPa)	$\sigma_{t,max}$ (MPa)	$\varepsilon_{t,c}$ (%)	$\varepsilon_{t,max}$ (%)
UHPC_0%	5.65 *(17%)*	5.65 *(17%)*	0.037 *(28%)*	0.037 *(28%)*
UHPFRC_0.6%	3.74 *(17%)*	4.49 *(14%)*	0.029 *(31%)*	0.07 *(19%)*
UHPFRC_1.25%	4.90 *(5%)*	5.40 *(6%)*	0.035 *(17%)*	0.20 *(43%)*
UHPFRC_1.9%	3.93 *(14%)*	5.88 *(17%)*	0.036 *(25%)*	0.56 *(5%)*
UHPFRC_2.55%	6.14 *(14%)*	8.11 *(10%)*	0.062 *(34%)*	0.87 *(40%)*

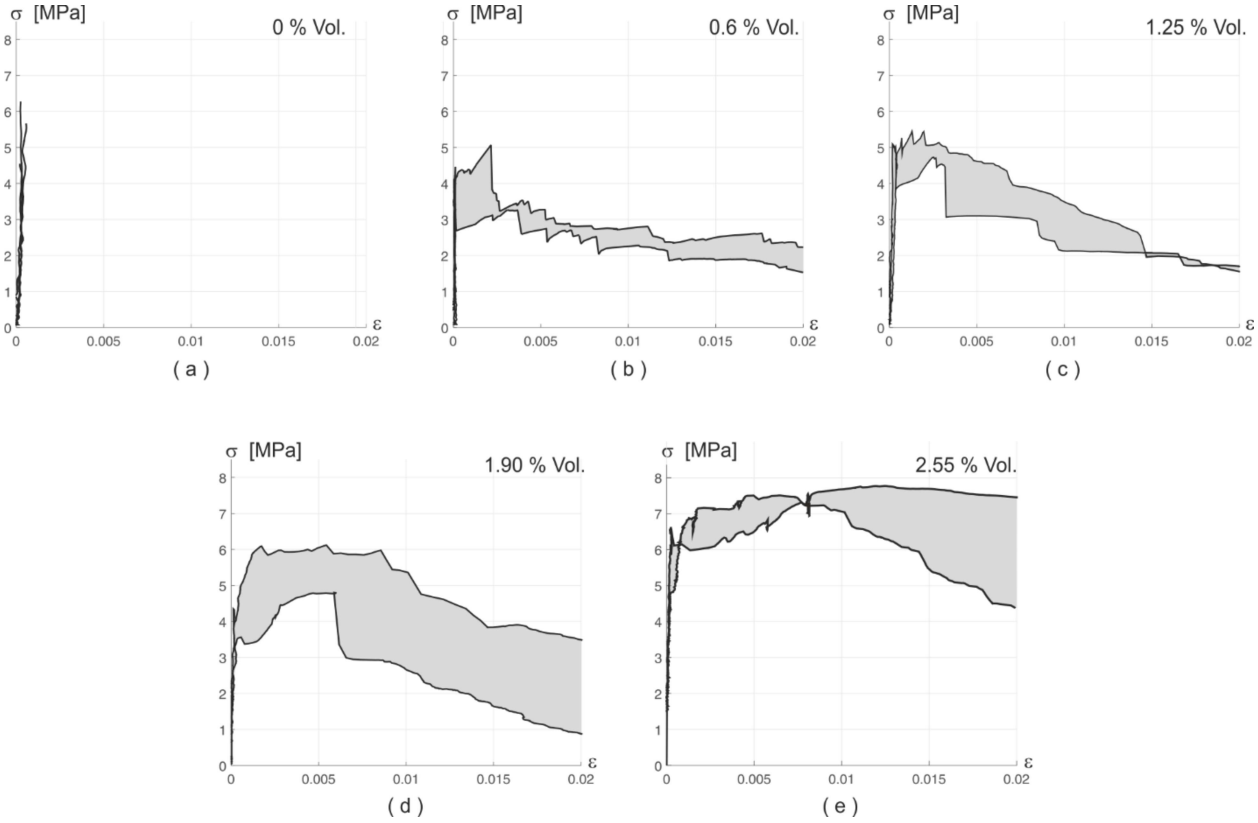

Figure 5. Stress-strain curves of direct tensile tests on dog-bone shaped specimens.

Fig. 5 shows the tensile stress-strain curves of UHPFRC with different amount of hooked steel fibers. Specimens without fibers (UHPC) showed a linear elastic behavior in tension up to failure

(Fig. 5a), with the formation of a single pass-through crack. Failure was brutal, after the formation of one unique crack.

The addition of hooked steel fibers, even at the lowest dosage (0.6% by volume), was able to avoid brutal failure and allowed the specimen to undergo plastic deformation after the formation of the first crack (Fig. 5b). An increase in the fibers volume from 0.6 to 2.55% results in an increase of the tensile strength of the composite $\sigma_{t,max}$ from 4.5 to 8.1 MPa, as well as an increase in the maximum post-cracking strain $\varepsilon_{t,max}$ from 0.07 to 0.87%. The bridging action provided by steel fibers across the cracks was manifested in all the samples, regardless of the amount of fibers used.

It is interesting to note that the post-cracking behavior changed by varying the fibers volume fraction. Looking at the stress-strain curves, for low dosages of steel fibers (0.6% and 1.25%) a strain-softening behavior is observed after the formation of the first crack (Figs. 4b,c), while in specimens reinforced with higher dosages of fibers (1.9% and 2.55%) the post-cracking behavior changed from strain-softening to strain-hardening (Figs. 5d,e).

For low fibers dosage (0.6% or 1.25%) only one or two visible cracks formed within the specimen cross-section (Fig. 6a), and one of them propagated and continued to grow in the strain-softening branch up to failure. In this phase, the stress-strain curve can be no longer expressed as a function of average deformation but rather as localized deformation. The amount and shape of steel fibers govern the slope and length of the strain-softening branch. In this study the use of hooked steel fibers guaranteed a long softening branch and a slight load decrease, due to limited slippage of fibers within the concrete matrix. The non-homogeneous fibers distribution observed in specimens with low fibers content (see UHPFRC_0.6% and UHPFRC_1.25% in Table 4) may have caused a non-uniform stress distribution across the specimen section, thus reducing the slope of the stress-softening branch (which in fact is lower than that of numerical simulations).

The post-cracking behavior changed when a certain threshold in the fibers volume fraction was exceeded (a value between 1.25% and 1.9%), leading to the formation of multiple cracks along the entire length of the specimen (Figs. 6b) and a shift from strain-softening to strain-hardening behavior. The fibers volume that allows to obtain a strain-hardening behavior, in the case of hooked steel fibers, is usually equal to or greater than 2%, as also confirmed by other studies from the literature for different UHPFRC mixtures [19,21].

The tensile stress at first cracking ($\sigma_{t,c}$) did not show any improvement by increasing the fibers volume fractions. On the contrary, when a low fibers dosage was used, the formation of the first crack was reached at lower tensile stresses with respect to the plain UHPC specimen. This was probably due to a bad dispersion and to some segregation of the fibers within the cross-section (see the cross-section of UHPFRC_0.6% in Table 4) that might have constituted a discontinuity, or to the presence of some air voids that reduced the resistant section and anticipated the formation of the first crack (see the cross-section of UHPFRC_1.9% in Table 4). Only when the highest dosage of fibers was used (UHPFRC_2.55%) the tensile strength at first cracking increased, since the high amount of fibers was able to counteract the possible presence of defects in the matrix.

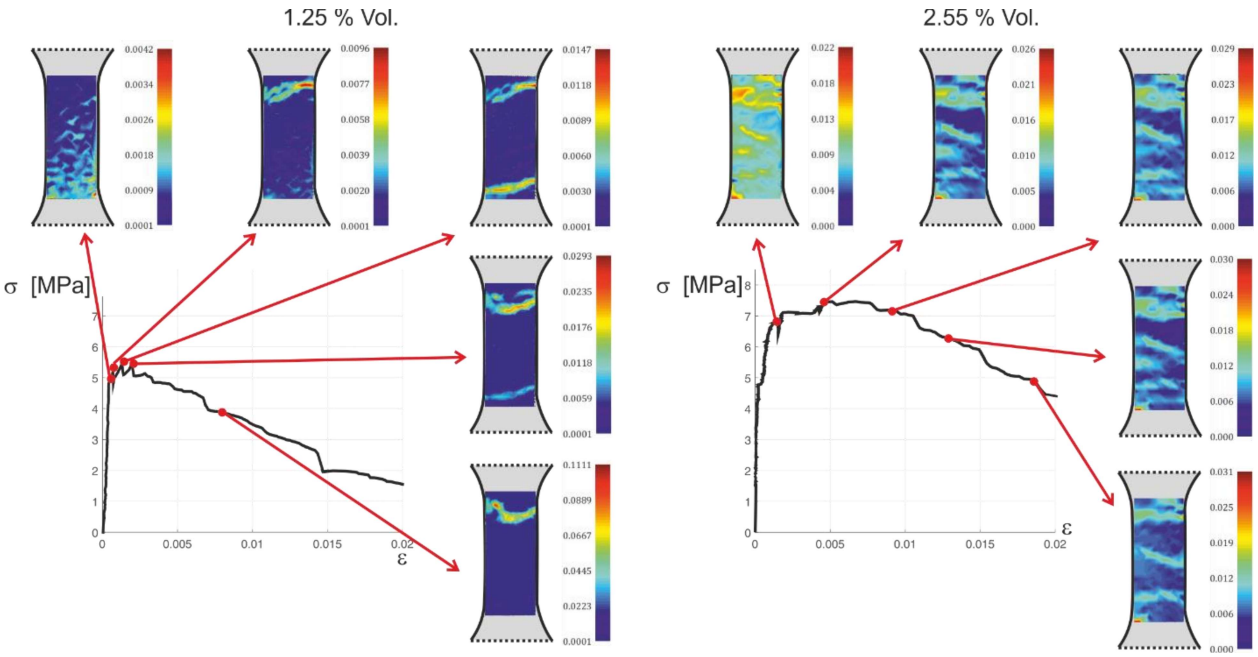

Figure 6. Frontal strain map of dog-bone shaped specimens at different steps of the stress-strain curve: (a) UHPFRC_1.25%, (b) UHPFRC_2.55%.

4. Variational model

The general theoretical principles governing the theory used to formulate the variational model are briefly recalled in this section. These principles are referred to the case of a mixture constituted by brittle and elasto-plastic phases, describing the cementitious matrix and the reinforcing fibers of UHPFRC composites, respectively.

The following notation is used. Scalar quantities are denoted by italic letters, while vectors and tensors are denoted by boldface letters (lower-case for vectors and upper-case for tensors). A superposed dot indicates derivative with respect to time t, $df(t)/dt = \dot{f}(t)$.

Let $\mathbf{s}=\mathbf{s}(x,t)$ be the list of state variables defined at any point x of the body Ω, and at any time instant $t \geq 0$ of the evolution process. The total internal energy of Ω is $W = W(\mathbf{s})$, and the external work expended in the time interval $[0,t]$ is $L = L(t)$. The set of equations that govern the evolution process are deduced by three principles, which are listed below, according to the energetic formulation for rate independent systems [49].

1. *Stability condition*. It is a local directional stability condition, which states that a state $\mathbf{s}$ is stable if, for any admissible state $\tilde{\mathbf{s}}$, a scalar $\tilde{h} > 0$ exists, such that for any $h \in [0, \tilde{h}]$

$$W(\mathbf{s}) \leq W(\mathbf{s} + h\tilde{\mathbf{s}}).$$

A necessary condition for the above inequality to be satisfied is that the first variation of W be non-negative for any admissible perturbation, i.e.,

$$\delta W(\mathbf{s})[\tilde{\mathbf{s}}] \geq 0, \quad \forall \tilde{\mathbf{s}}. \qquad \text{(SC)}$$

2. *Energy balance*. It states that for any t, the internal energy expended in the interval $[0,t]$ is equal to the external work expenditure

$$W(\mathbf{s}(t)) - W(\mathbf{s}(0)) = L(t),$$

which is equivalent to the energy rate balance equation

$$\dot{W}(\mathbf{s}(t)) - \dot{L}(t) = 0. \qquad \text{(EB)}$$

3. *Dissipation (irreversibility) conditions*. Certain irreversibility conditions are assigned, such as the condition that damage cannot reduces in an evolution process. These constrains guarantee the fulfilment of the second law of thermodynamics.

4.1 1D formulation

In this section, the model is deduced from the three principles of stability, energy balance and dissipation, in the one-dimensional case of a tensile bar. The simplified 1D setting is proposed for three reasons.

1. Although the 1D hypothesis represents a drastic geometrical restriction, however it preserves the key modelling aspects, providing a thorough mechanistic understanding of the model predictive possibilities.
2. The 1D format can be easily extended to the general 3D framework. The reader interested in the 3D formulation can refer to [33], where the model is first deduced in the general multi-dimensional case, and, then, it is adapted to the 1D problem.
3. Calibration formulas are deduced from the 1D problem and used to assign the model parameters. They are based on experimental data, which can be easily determined from the tensile tests discussed in the previous sections.

In the following, indices *m* and *r* are used to refer quantities to matrix and reinforcement phase, respectively. Furthermore, a prime is used either for derivative with respect to the spatial coordinate *x*, and for derivative with respect to the argument of the function, i.e. $df(x,t)/dx = f'(x,t)$, or $df(y)/dy = f'(y)$.

Geometry, variables and boundary conditions. The geometrical scheme of the 1D problem is plotted in Fig. 7(a). A bar of length *L* is composed by two parallel sub-bars, representing the two composite phases (matrix (gray bar) and reinforcement (blue bar)), which are connected by elastic springs. The longitudinal coordinate through the bar is $x \in (0, L)$. Displacements of matrix and reinforcement phases are $u_m = u_m(x)$ and $u_r = u_r(x)$, respectively. Fracture in the matrix phase is described by the damage field $d = d(x) \in [0,1]$, where *d*=0 means sound material, and *d*=1 means fractured material, as usually assumed in damage models. To avoid material self-healing, damage satisfies the irreversibility condition

$$\dot{d} \geq 0. \qquad (1)$$

The plastic strain in the reinforcement is denoted by $\varepsilon_p = \varepsilon_p(x)$, and the cumulated plastic strain is

$$p = \int_0^t |\dot{\varepsilon}_p| \, dt, \qquad (2)$$

as typically defined in plasticity.

Summing up, the variables vector is $\mathbf{s} = (u_m, u_r d, \varepsilon_p, p)$.

Strains in the two phases are $\varepsilon_m = u_m'$ and $\varepsilon_r = u_r'$, with ε_r sum of plastic contribution ε_p and elastic contribution $\varepsilon_r - \varepsilon_p$. Conditions at the bar's endpoints are

$$\begin{aligned} &u_m(0) = u_r(0) = 0, \qquad u_m(L) = u_r(L) = \varepsilon(t)L, \\ &d(0) = d(L) = 0, \qquad \varepsilon_p(0) = \varepsilon_p(L) = 0, \end{aligned} \qquad (3)$$

where the assigned deformation $\varepsilon = \varepsilon(t)$ is a monotonical increasing function of time *t*, with $\varepsilon(0) = 0$.

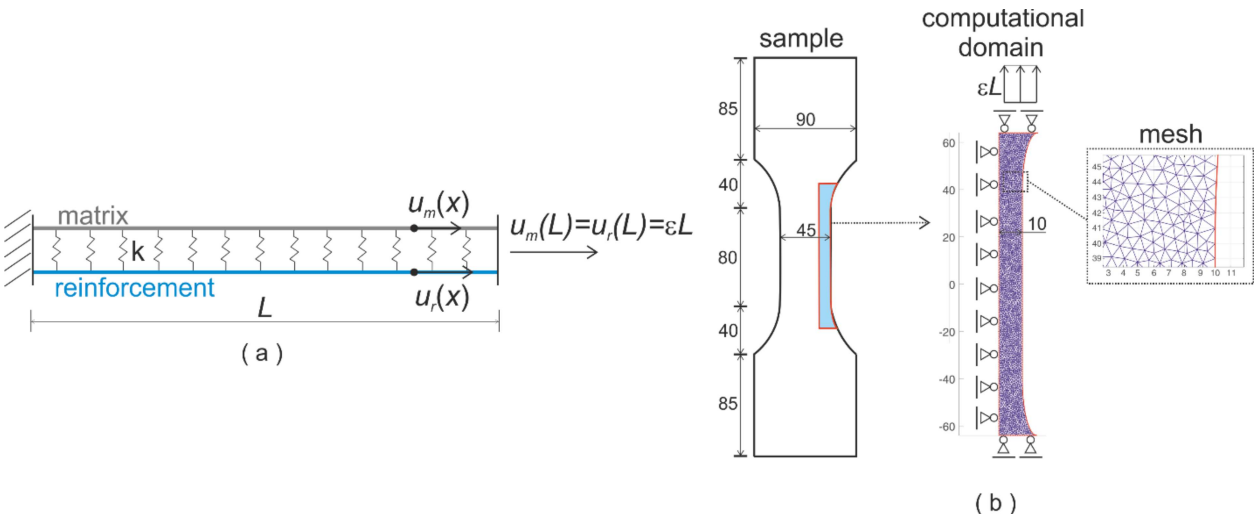

Figure 7. (a) Geometrical scheme of 1D problem. (b) Geometry and mesh of 2D problem.

Energies and stresses. The internal energy of the bar is

$$W(u_m,u_r d,\varepsilon_p,p)=\int_0^L\left[v_m E_m(u_m,d)+v_r E_r(u_r,\varepsilon_p,p)+E_b(u_m,u_r)\right]dx, \tag{4}$$

where E_m, E_r and E_b are the energy densities of matrix, reinforcement, and interface, respectively, whose expressions are specified in the following, and v_m and v_r are the volume fraction of matrix and reinforcement phases.

1. The matrix energy density has the expression usually assumed in phase-field models of fracture [34,50]

$$E_m(u_m,d)=\frac{1}{2}(1-d)^2E_m u_m'^2+\frac{\bar{\sigma}_m^2}{E_m}\left(d+\frac{1}{16}l_m^2 d'^2\right), \tag{5}$$

where the first term is the matrix elastic energy density, with E_m the matrix Young's modulus, and the second term is the damage energy term, which is sum of local and non-local contributions, depending on damage and on damage first derivative, respectively. The function $(1-d)^2$ in the first term is the so-called degradation function. It produces a reduction of the elastic energy density when d increases. The damage energy depends on the peak stress $\bar{\sigma}_m$, at which damage initiates, and on the internal length l_m, representing the width of the zone where damage localizes (process zone size).
Since the local damage term is a linear function of d, the functional (5) is usually labeled by the acronym AT1, where the letters AT recall the names of Ambrosio and Tortorelli, who first introduced an analogous functional to regularized free-discontinuities problems [51,52], and the number 1 refers to the fracture energy first order dependence on d.

2. The reinforcement energy density is

$$E_r(u_r,\varepsilon_p,p)=\frac{1}{2}E_r\left(u_r'-\varepsilon_p\right)^2+w(p)+\frac{1}{2}w_r l_r^2 p'^2, \tag{6}$$

where the first term is the elastic energy density, with E_r the reinforcement Young's modulus, and the second and third terms are plastic energies, depending on the cumulated plastic strain p (local contribution) and on its derivative p' (non-local contribution). The

elastic energy depends on the elastic strain $\left(u_r' - \varepsilon_p\right)$. The local plastic energy is a convex-concave function whose expression is

$$w(p) = \begin{cases} \frac{1}{2}\frac{\hat{\sigma}_r - \bar{\sigma}_r}{\hat{p}} p^2 + \bar{\sigma}_r p, & \text{if } 0 < p \le \hat{p}, \\ -\frac{1}{2} S(p-\hat{p})^2 + \hat{\sigma}_r (p-\hat{p}) + w(\hat{p}), & \text{if } p > \hat{p}, \end{cases} \tag{7}$$

where $\bar{\sigma}_r$ is the plastic yield stress, $\hat{\sigma}_r$ is the peak stress at which the softening regime initiates, and S is the softening modulus. Graphs of $w(p)$ and its derivative is drawn in Fig. 8. The plastic response strongly depends on the convexity properties of w [35–37]. If w is convex, the plastic strain diffuses within the body in regime of hardening, while, if w is concave, the plastic strain localizes in portions of the body in regime of softening. In this latter case, the width of the localization band is equal to the internal length l_r, appearing in the non-local plastic energy. The second coefficient w_r of the non-local plastic energy is calibrated by a specific formula deduced in [36] and proposed in the next Sect. 4.2. Aifantis's gradient plasticity theory [53,54] is variationally deduced from functional (6) (see [55,56]).

3. Finally, material phases are connected by elastic springs, whose energy density is

$$\mathsf{E}_b(u_m, u_r) = \frac{1}{2}\frac{E_b}{l_b^2}\left(u_m - u_r\right)^2, \tag{8}$$

which is a quadratic expression of the relative displacement $\left(u_m - u_r\right)$ between phases. The springs' elastic coefficient is written as ratio E_b/l_b^2, where E_b is an elastic modulus, and l_b is an internal length. The mechanical meaning of l_b, and the expression of E_b are given in the next Sect. 4.2.

We point out that damage and plastic local energies are dissipative since their time derivatives are non-negative

$$\frac{d}{dt}\left(\hat{\sigma}_m^2 d / E_m\right) = \hat{\sigma}_m^2 \dot{d} / E_m \ge 0, \qquad \frac{d}{dt} w(p) = w'(p)\dot{p} \ge 0. \tag{9}$$

Furthermore, since external loads are assumed to be null, the internal energy coincides with the bar's total energy.

Normal stresses within each phase are obtained by differentiating the elastic energy densities with respect to strain, and the shear force exchanged by phases is obtained by differentiating the bond energy density

$$\sigma_m = (1-d)^2 E_m \varepsilon_m, \qquad \sigma_r = E_r(\varepsilon_r - \varepsilon_p), \qquad \tau = \frac{E_b}{l_b^2}(u_m - u_r). \tag{10}$$

The total stress is

$$\sigma = v_m \sigma_m + v_r \sigma_r. \tag{11}$$

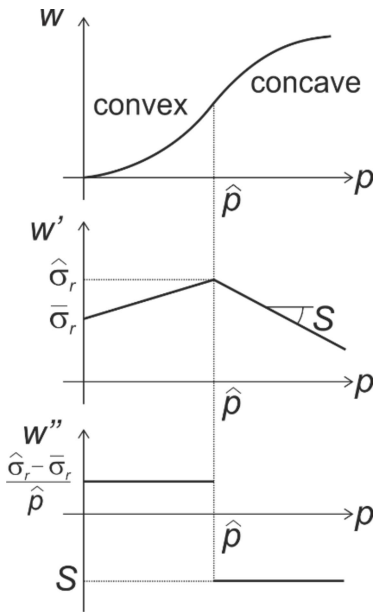

Figure 8. Graphs of plastic energy density and its derivatives.

Equilibrium. Equilibrium relations are obtained from the first-order stability condition (SC). By requiring the first variation of the energy to be non-negative, and following the standard variational procedure, we obtain

1. the macroscopic balance equations
$$v_m \sigma_m' - \tau = 0, \qquad v_r \sigma_r' + \tau = 0, \tag{12}$$
for each phase, which are coupled by the exchanging shear stress τ;
2. the fracture yield condition
$$|\sigma_m| \le \hat{\sigma}_m \sqrt{(1-d)^3 (1 - l_m d'')} := \sigma_{m,y}(d), \tag{13}$$
which states that the stress in the matrix cannot exceed the damage yielding stress $\sigma_{m,y}$. Since $\sigma_{m,y}(0) = \hat{\sigma}_m$, the stress $\hat{\sigma}_m$ is the stress at which damage can form;
3. the plastic yield condition
$$|\sigma_r| \le w'(p) - w_r l_r^2 p'' := \sigma_{r,y}(p), \tag{14}$$
where the plastic yielding stress $\sigma_{r,y}$ is an upper bound for the stress in the reinforcement. Since $\sigma_{r,y}(0) = w'(0) = \bar{\sigma}_r$, $\bar{\sigma}_r$ represents the yield stress at which plastic strains can initiate and, eventually, develop.

Consistency conditions. The following consistency conditions are obtained from the energy balance (EB)

$$\left(\sigma_{m,y}^2 - \sigma_m^2\right)\dot{d} = 0, \qquad \left(\sigma_{r,y} - \operatorname{sign}(\dot{\varepsilon}_p)\sigma_r\right)\dot{p} = 0, \tag{15}$$

which state that damage and plastic strain growth, i.e., $\dot{d} > 0$ and $\dot{p} > 0$, only if $|\sigma_m| = \sigma_{m,y}$ and $|\sigma_r| = \sigma_{r,y}$, respectively. Being $\dot{\varepsilon}_p = \operatorname{sign}(\dot{\varepsilon}_p)\dot{p}$, equation $(15)_2$ leads to the plastic flow rule $\dot{\varepsilon}_p = \operatorname{sign}(\sigma_r)\dot{p}$. Accordingly, if we restrict to the case of tensile tests for which $\sigma_r \ge 0$, we get $\dot{\varepsilon}_p = \dot{p}$, and, thus, ε_p coincides with p, and one of the two variables can be skipped.

Remarks on the evolution process. In a process, which starts from the initial undeformed and unfractured state ε=0, and evolves according to the deformation ε that monotonically increases, the bar experiences an initial uniform elastic stretching, with $\varepsilon_m = \varepsilon_r = \varepsilon(t)$. The elastic stage terminates in two possible ways:

1. the stress $\sigma_m = E_m \varepsilon$ in the matrix reaches the peak value $\widehat{\sigma}_m$, and a first crack forms;
2. the stress $\sigma_r = E_r \varepsilon$ in the reinforcement attains the yielding stress $\overline{\sigma}_r$, and the plastic strain initiates and evolves.

Since in tensile tests on UHPFRC fractures open into the matrix only after the purely elastic stretching, the condition

$$\overline{\sigma}_r \geq \frac{E_r}{E_m} \widehat{\sigma}_m \tag{16}$$

must be fulfilled. The strain and stress pair $(\varepsilon_0, \sigma_0)$ at which the first crack opens (see Fig. 9a) is

$$\varepsilon_0 = \frac{\widehat{\sigma}_m}{E_m}, \qquad \sigma_0 = \frac{v_m E_m + v_r E_r}{E_m} \widehat{\sigma}_m. \tag{17}$$

The first crack opening, and all the subsequent fracture openings, are accompanied by stress drops (see the numerical stress-strain curves of Fig. 11b,c), which are followed by increasing stress-strain branches. The hardening behavior in between consecutive stress drops is due to the fibers bridging action. The stress in the fibers significantly increases around cracks, leading to the development of plastic strains, and it is gradually transferred from fibers to matrix within the so-called "stress transfer zone". On the contrary, the matrix stress decreases in the stress transfer zone, going to zero in correspondence of cracks. New cracks form when the peak stress $\widehat{\sigma}_m$ is attained at points which are typically placed in between preexisting cracks. The saw-tooth stress-strain branch of Fig. 11b,c corresponds to this process of progressive formation of cracks, which ends when the peak stress $\widehat{\sigma}_r$ is reached in the reinforcement at a certain crack. The reinforcement enters the plastic strain-softening regime, and the plastic strain progressively localizes around that crack. This process leads to bar's failure.

We noticed that in order to have a strain-hardening process of multi-cracking, in which multiple cracks progressively open, it must be

$$\widehat{\sigma}_r > \frac{\sigma_0}{v_r}. \tag{18}$$

4.2 Parameters calibration

The model parameters can be calibrated based on experimental data which can be easily measured in a tensile test performed on a sample with a specific amount of fibers. Here, we consider 2.55 % Vol. of fibers. The experimental data required to calibrate the model parameters can be extracted by a stress-strain curve and by a strain contour map, made by DIC technique. They are drawn in Fig. 9a,b, selected as the most representative of experimental results on 2.55 % Vol. fiber samples. Quantities directly used for calibration are highlighted in red color, and their values are ε_0=0.133*10^{-3}, σ_0=5.75 MPa, ε_{peak}=1.2*10^{-3}, σ_{peak}=7.95 MPa, E_s=8.5*10^{-3} MPa, l_r=10 mm, and l_b=15 mm.

In the following, we enumerate each single constitutive parameter of the model, indicating the strategy to calibrate it, and giving its value based on the above experimental data.

i. Young's modulus of concrete E_m. In this study, the elastic modulus E_m has been estimated by using the simplified formula proposed by [1,21]

$$E_m = k_0 * f_c^{1/3}$$

Where f_c is the concrete compressive strength and k_0 can be assumed equal to 9000. According to that, E_m is about $40*10^3$ MPa.

ii. Young's modulus of reinforcement E_r. It differs from the modulus of each single steel fiber, since it accounts for the overall effect of fibers embedded into the matrix. Fibers are assumed to be homogeneously distributed with random orientation to ensure an isotropic response. It can be determined from (17). Indeed, by inverting it, we obtain

$$E_r = \frac{1}{v_r}\left(\frac{\sigma_0}{\varepsilon_0} - v_m E_m\right). \tag{19}$$

For the application at hand, its value is $E_r=170*10^3$ MPa.

For the fracture energy of the matrix phase, the parameters to be assigned are l_m and $\hat{\sigma}_m$.

iii. The internal length l_m, measures the size of the process zone of micro-cracks (see [50] for the analytical justification). It is assumed to be 2-3 times the maximum size of concrete aggregates (in general, 2-3 times the size of the matrix constituent grains [57]). We assume l_m=1 mm.

iv. The fracture stress $\hat{\sigma}_m$ is determined by inverting equation $(17)_2$

$$\hat{\sigma}_m = \frac{E_m}{v_m E_m + v_r E_r}\sigma_0. \tag{20}$$

The resulting value is $\hat{\sigma}_m = 5.31$ MPa. In the simulations presented in the next Sect. 5, the matrix peak stress $\hat{\sigma}_m$ has been perturbed through a random function of amplitude 1% to account for material inhomogeneity. The perturbation reduces the possibility that multiple cracks simultaneously open, promoting the formation of single cracks at a time.

Regarding the plasticity parameters, the following parameters are assigned. They differ from those of a single fiber, because they account for the overall response of homogeneously distributed and randomly oriented fibers.

v. Plastic yield stress $\bar{\sigma}_r$. The stress $\bar{\sigma}_r$ must satisfies inequality (16). Since $E_r\hat{\sigma}_m/E_m = 22.5$ MPa, we assume the value $\bar{\sigma}_r = 50$ MPa. Not reported simulations have shown that different values of $\bar{\sigma}_r$ within the range $25 < \bar{\sigma}_r < 75$ MPa do not significantly modify the numerical results.

vi. Peak stress $\hat{\sigma}_r$. It is assigned by using inequality (18). Let $v_{r,\min}$ be the reinforcement volume fraction for which inequality (18) is satisfied as an equality

$$\hat{\sigma}_r = \sigma_0 / v_{r,\min}. \tag{21}$$

The volume fraction $v_{r,\min}$ is the minimum amount of fibers that allows for a hardening process of multi-cracking (although small). For $v_r > v_{r,\min}$, a tensile samples experiences multi-cracking in strain-hardening regime (*ductile failure*), while, for $v_r < v_{r,\min}$, the sample undergoes a single crack opening, and a softening stage, which directly follows the elastic phase (*quasi-brittle failure*). The graph of function $\hat{\sigma}_r/\sigma_0 = 1/v_{r,\min}$ is plotted in Fig. 9c, and the two ductile and brittle branches are distinguished by different colors. Experiments have shown that $v_{r,min}$ is between v_r=0.0125 and v_r=0.0190. If we assume $v_{r,min}$=0.0185, from (21) we have $\hat{\sigma}_r = 312$ MPa.

vii. The plastic strain $\hat{p}$ corresponding to $\hat{\sigma}_r$ is related to the mean plastic strain, which is practically equal to ε_{peak} of Fig. 9a. Since at the end of the multi-cracking stage, p is not homogeneous through the bar, localizing across the cracks, where it attains the maximum values $\hat{p}$, the inequality $\hat{p} = \max(p(x)) > \text{mean}(p(x)) \simeq \varepsilon_{peak}$ holds. Thus, a value of $\hat{p}$ larger than ε_{peak} should be assigned. Accordingly, we assign $\hat{p}$ =1.4*10^{-3} (larger than ε_{peak}=1.2*10^{-3}).

viii. Internal length l_r. The size of the band where the plastic strain localizes in the phase of macro-cracking is related to the fiber's length. This size can be directly measured form the strain contour maps of Fig. 9b, where its value is about l_r=10 mm.

ix. The softening coefficient S of the plastic energy density (7), and the coefficient w_r of the non-local plastic energy in (6). They are calibrated by using formulas (4.58) in [33], deduced from the analytical solution of the 1D elastoplastic problem [36]. They relate S and w_r to the slope E_s of the softening branch of the stress-strain curve (see Fig. 9a), and to other known quantities, like the Young's moduli, the bar's length L, and the internal length l_r

$$S = -E_S \frac{l_r}{L}\left(1 - \frac{E_S}{E_r}\right)^{-1}, \qquad w_r = \frac{S}{4\pi^2}. \tag{22}$$

The resulting values are S=-1.012*10^3 MPa, and w_r=25.63 MPa.

A simplified 1D problem was formulated and solved in [33] in order to characterize the parameters l_b and E_b of the interface energy density (8), and, then, to calibrate them. Here, we recall the main ideas of the model, referring to [33] for a detailed description. The model geometry is that drawn in Fig. 7a, considered for the 1D variational model of Sect. 4.1. The simplified model assumes that fracture and plasticity localize at points (differently, fracture and plasticity are smooth field variables in the variational model), according to the following constitutive assumptions.

1. Fractures open in the matrix at points where the peak stress $\hat{\sigma}_m$ is exceeded.
2. The reinforcement admits the development of plastic hinges at points where fractures are opened in the brittle phase, and the plastic displacement Δ at each skate evolves according to the bilinear hardening-softening expression

$$\sigma_r = \begin{cases} \dfrac{\hat{\sigma}_r - \bar{\sigma}_r}{\hat{\Delta}}\Delta + \bar{\sigma}_r, \text{ if } 0 < \Delta \le \hat{\Delta}, \\ -S(\Delta - \hat{\Delta}) + \hat{\sigma}_r, \qquad \text{if } \Delta > \hat{\Delta}. \end{cases} \tag{23}$$

This stress-displacement law is the first derivative of the plastic energy (7), with p replaced by Δ.

3. The bond elastic springs exchange the shear force $(10)_3$ between the two phases.

For an increasing deformation ε, the evolution problem is solved analytically in the simplified case that cracks always maintain equidistant. Accordingly, we suppose that, at a certain instant of the evolution process, n equally spaced fractures have opened in the bar, and that plastic hinges have formed at fracture points, and they have experienced the plastic displacement Δ. The equilibrium configuration can be determined by solving the equilibrium equations (12) and the kinematical compatibility equation

$$\varepsilon L = 2n\int_0^l \varepsilon_r(x)dx + n\Delta, \tag{24}$$

where the first term on the right side is the stretching of the sound parts, with $l = L/(2n)$, and the second term accounts for displacement at plastic hinges. The analytical solution has been found in [33], which we refer to for the explicit expression of the solution at any instant of the evolution process.

At equilibrium, the distributions of σ_m and σ_r within any sound portion of the bar have the profiles shown in Fig. 10. The maximum stress $\sigma_m^{\max}$ in the matrix is attained at midpoint, while the maximum stress $\sigma_r^{\max}$ in the reinforcement phase is reached at fracture points. In order to characterize the constitutive parameters l_b and E_b, we suppose that, at a certain instant of the evolution,

$$\sigma_m^{\max} = \hat{\sigma}_m, \quad \sigma_r^{\max} = \hat{\sigma}_r. \tag{25}$$

The first equation states that the crack opening at midpoint of the sound portion of the bar is incipient, and the second equation says that plastic hinges are going to enter the softening plastic regime. If the first event happens, a new crack forms and the crack spacing halves, reducing to l, which is the minimum spacing that can be achieved at the end of the hardening stage.

We assume that the internal length l_b is the distance between adjacent crack at the end of the microcracking process, which can be measured from experiments (see Fig. 9b). Under this assumption, the analytical solution of [33], allows to determine the expression of the modulus E_b such that equations (25) be satisfied with $l=l_b$, which is

$$E_b = \left(\operatorname{arcsech}\left(1-(1+\frac{v_m E_m}{v_r E_r})\frac{E_m \hat{\sigma}_m}{E_r \hat{\sigma}_r} \right) \right)^2 \Bigg/ \left(\frac{1}{v_m E_m} + \frac{1}{v_r E_r} \right), \tag{26}$$

And it depends on known parameters. With this value, the softening stage of macro-crack evolution initiates when the spacing between adjacent micro-cracks is at least equal to l_b.

Using the above calibration criteria, we set l_b=15 mm, and, from (26), E_b=14.96*10^3 MPa.

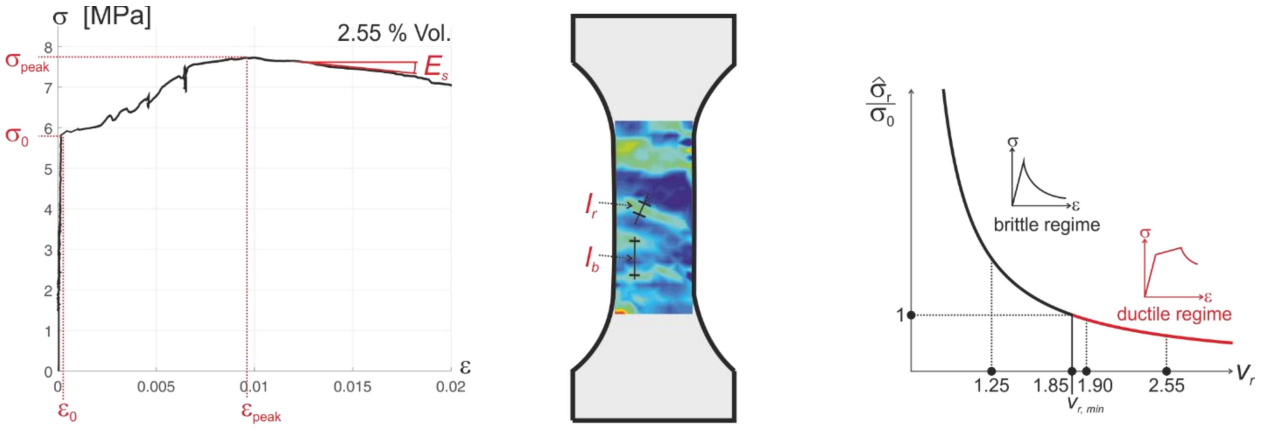

(a) (b) (c)

Figure 9. Data from tensile tests that are needed for model calibration: (a) stress-strain curve and (b) strains map at failure for fibers volume fraction 2.55 % Vol.; (c) curve $\hat{\sigma}_r/\sigma_0 = 1/v_{r,\min}$, marking ductile and brittle failure regimes.

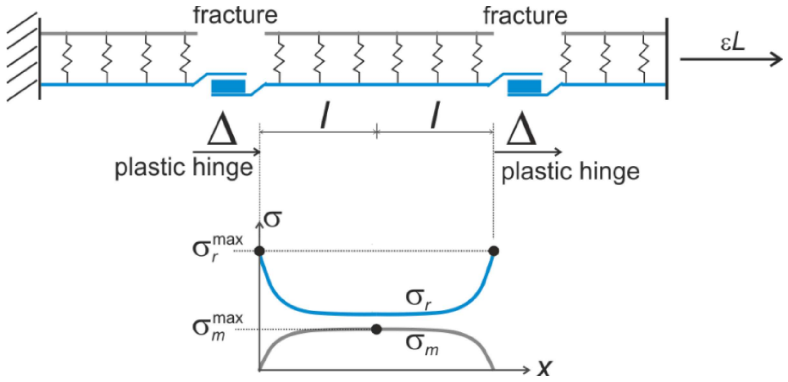

Figure 10. Geometrical scheme of the analytical model developed to characterize l_b and E_b, and stresses profiles in a portion between adjacent cracks.

4.3 3D formulation

In this section, we recall the main equations that govern the evolution problem in the general 3D setting (see [33] for a detailed description).

Let Ω be a three-dimensional body, with points $x \in \Omega$. We define the state variables vector $\mathbf{s} = (\mathbf{u}_m, \mathbf{u}_r, d, \mathbf{P}, p)$, which collects the displacements $\mathbf{u}_m = \mathbf{u}_m(x)$ and $\mathbf{u}_r = \mathbf{u}_r(x)$ of matrix and reinforcement, the fracture variable $d = d(x)$, the plastic strain tensor $\mathbf{P} = \mathbf{P}(x)$, which is assumed to be symmetric, and the cumulated plastic strain $p = \int_0^t |\dot{\mathbf{P}}|\, dt$.

The internal energy of Ω is

$$\mathsf{E}(\mathbf{s}) = \int_\Omega \left\{ v_m \left((1-d)^2 \varphi_m(\mathbf{E}_m) + \frac{\bar{\sigma}_m^2}{E_m} \left(d + \frac{1}{16} l_m^2 \nabla^2 d \right) \right) + v_r \left(\varphi_r(\mathbf{E}_r - \mathbf{P}) + w(p) + \frac{1}{2} w_r l_r^2 \nabla^2 p \right) + \frac{1}{2} \frac{E_b}{l_b^2} (\mathbf{u}_m - \mathbf{u}_r)^2 \right\} dx \tag{27}$$

where

$$\varphi_i(\mathbf{E}) = \mu_i \mathbf{E}^2 + \frac{1}{2} \lambda_i \mathrm{tr}(\mathbf{E})^2, \quad i = m, r \tag{28}$$

are the elastic energy densities of matrix and reinforcement, with $\mathbf{E}_i = sym \nabla \mathbf{u}_i$ the strain tensor, and μ_i and λ_i the Lamè's parameters. We notice that the damage and plastic energy densities are equal to the densities of the 1D formulation (see the energy densities (5) and (6)), since they still depend on scalar fields, i.e., the damage field d and the cumulated plastic strain field p. The convex-concave expression (7) is assumed for the local plastic energy density. Stress tensors of the two phases and the bond force are

$$\mathbf{T}_m = (1-d)^2 \frac{d\varphi_m(\mathbf{E}_m)}{d\mathbf{E}_m}, \quad \mathbf{T}_r = \frac{d\varphi_r(\mathbf{E}_r)}{d\mathbf{E}_r}, \quad \boldsymbol{\tau} = \frac{E_b}{l_b^2} (\mathbf{u}_m - \mathbf{u}_r). \tag{29}$$

The equilibrium equations are deduced from (SC), and they are

$$v_m \mathrm{div} \mathbf{T}_m - \boldsymbol{\tau} = 0, \quad v_r \mathrm{div} \mathbf{T}_r + \boldsymbol{\tau} = 0,$$

$$f_m(\mathbf{u}_m, d) := 2(1-d)\varphi_m(\mathbf{E}_m) + \frac{\bar{\sigma}_m^2}{E_m} \left(\frac{1}{8} l_m^2 \Delta d - 1 \right) \le 0, \tag{30}$$

$$f_p(\mathbf{u}_r, \mathbf{P}, p) := |\mathbf{T}_r(\mathbf{u}_r, \mathbf{P})| - \frac{dw}{dp}(p) + w_r l_r^2 \Delta p \le 0,$$

and they represent the 3D counterpart of (12), (13) and (14), respectively. The energy balance equation (EB) provides the consistency conditions

$$f_m(\mathbf{u}_m, d)\dot{d} = 0, \quad f_p(\mathbf{u}_r, \mathbf{P}, p)\dot{p} = 0, \tag{31}$$

and, in addition, the plasticity flow rule

$$\dot{\mathbf{P}} = \dot{p}\mathbf{N}_r, \quad \text{with} \quad \mathbf{N}_r = \frac{\mathbf{T}_r}{|\mathbf{T}_r|} = \frac{\partial f_r}{\partial \mathbf{T}_r}, \tag{32}$$

which is typical of associative plasticity.

4.4 Evolution problem

Hereinafter, the evolution problem, formulated as an incremental minimum problem, is briefly presented, and the reader is referred to [33] for an in-depth description. Time t is discretized into finite intervals of size τ, and, within each time step $t \to t + \tau$, the variable vector is approximated by the linear expressions

$$\mathbf{s}(x, t+\tau) = \mathbf{s}(x,t) + \tau\dot{\mathbf{s}}(x,t), \tag{33}$$

and the energy (4) (or (27)) for the 1D (or 3D) formulation is developed up to the second order, around the configuration $\mathbf{s}(x,t)$,

$$E(\mathbf{s}(x,t+\tau)) = E(\mathbf{s}(x,t)) + \tau\dot{E}(\mathbf{s}(x,t), \dot{\mathbf{s}}(x,t)) + \frac{1}{2}\tau^2\ddot{E}(\mathbf{s}(x,t), \dot{\mathbf{s}}(x,t)), \tag{34}$$

which can be rewritten as sum of a constant term and a quadratic functional of $\dot{\mathbf{s}}$ in the form

$$E(\mathbf{s}(x,t+\tau)) = \text{const} + \tau F(\dot{\mathbf{s}}(x,t)). \tag{35}$$

The configuration $\mathbf{s}(x,t+\tau)$ is determined by (33), with $\dot{\mathbf{s}}$ solution of the constrained minimum problem

$$\dot{\mathbf{s}}(x,t) = \arg\min\left\{F(\dot{\mathbf{s}}(x,t)), \quad \dot{d} \geq 0, \quad + \text{boundary conditions}\right\} \tag{36}$$

This problem is numerically solved by means of a finite element code which implements an iterative alternate minimization procedure, consisting in minimizing the energy functional with respect to the unknown fields separately, as thoroughly described in [33].

5. Results of numerical simulations

In this section, results of numerical simulations are presented and compared with experimental results. Both 1D and 3D problems are solved.

Geometry and finite elements discretization. For the 1D problem, a bar of length L=80 mm is considered, corresponding to the thinner central part of the dog-bone sample of Fig. 2, discretized by finite elements of size 0.25 mm. On each finite element, the variables u_m, u_r and d are approximated by quadratic shape functions based on three nodal values (at element endpoints and midpoint), and the variable ε_p is approximated by affine shape functions, depending on endpoints nodal values.

For the 3D problem, the hypothesis of plane stress state is assumed, thus reducing the problem to 2D. The domain considered in simulations is plotted in Fig. 7b. A portion of the domain is considered, which includes parts of the sample enlargements. A small portion is considered in order to limit the computational cost. Indeed, to accurately describe the process of damage and plastic strain localization, the mesh size must be smaller than the minimum internal length between l_m and l_r. Discretization is performed by an unstructured triangular mesh of size 1 mm, and reader is referred to the Appendix for an analysis of the effects of mesh size on the solution. On each element, variables $\mathbf{u}_m$, $\mathbf{u}_r$ and d are approximated by quadratic shape functions (six nodes quadratic

triangular element), and ε_p is approximated by affine shape functions (three nodes linear triangular element).

Results. Fig. 11 shows the stress-strain curves resulting from 1D (red line) and 2D (blue line) simulations for different fiber volume percentage. Curves capture the experimental results, reproducing the main phases of the evolution process. In case of 1.25 % Vol., after the initial elastic phase, a single crack forms in the domain (both in the 1D and 2D simulations), which produces a stress drop of the response curve. Then, after a very short strain-hardening phase due to the reinforcement capability of bridging stresses across the crack, the curve presents a long decreasing branch, as in experiments, associated to the progressive crack opening, that leads to the sample failure. In this phase, the reinforcement experiences plastic strain localization in a band across the crack. In the case of 1.90 and 2.55 % Vol., the initial elastic branch is followed by an increasing saw-tooth curve, which is related to the process of progressive multi-cracking. Each stress-drop corresponds to the opening of a single (sometimes double) crack, which always passes through the whole cross-section. The final softening branch corresponds to plastic strain localization across one of the pre-existing cracks. Although the numerical curves capture the key phases of the evolution process, nevertheless they also exhibit evident differences with the experimental curves. The presence of very pronounced stress drops is one of these differences. In simulations, stresses exhibit considerable discontinuities, because fractures always open brutally as lines that pass through the whole cross-section. Differently, in experiments, the crack patterning is much more irregular and fragmented. Small crack form and progressively evolve. Eventually, they merge with other cracks, and they branch in multiple cracks. This very gradual process of crack diffusion reflects on a more regular σ-ε curve, where the saw-tooth branch exhibits smaller stress discontinuities. This gradual process of multi-cracking is driven by the many inhomogeneities inherent in real experiments. Inhomogeneities are related to the material, such as inhomogeneous distribution of fibers, segregation of matrix components due to the casting process, or to the sample geometry, which can present imperfections, or to the test setup, where misalignments and loading eccentricities are inevitable. All these inhomogeneities are absent in simulations, where only the fracture stress $\hat{\sigma}_m$ has been slightly perturbed. This explain the process of abrupt passing-through fracture opening, captured by simulations and related to the pronounced stress drops of the σ-ε curves.

In the next subsection, the evolution of damage d and cumulated plastic strain p is analysed in the cases of 1.25 and 2.55 % Vol.. According to point iv. of Sect. 4.2, the sample undergoes quasi-brittle failure in the first case, since $v_r = 0.0125 < v_{r,\min} = 0.0185$, and ductile failure in the second case, being $v_r = 0.0255 > v_{r,\min} = 0.0185$. First, 1D numerical results are presented, and, then, 2D numerical simulations are discussed.

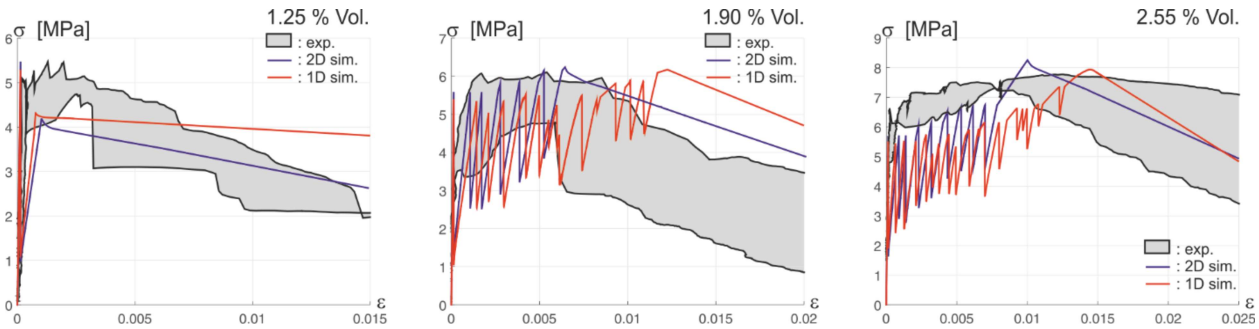

Figure 11. Stress-strain curves at three different fibers volumes. Comparison of experimental results (gray region), 1D simulations (blue curve) and 2D simulations (red curve).

5.1 1D tensile tests

Quasi-brittle failure. Profiles of d and p at two different instants of the evolution process (A and B) are plotted in Fig. 12 in the case of 1.25 % Vol. of fibers. A single crack opens into the bar at the stress drop of the response curve (ε=0.13*10^{-3}). It forms near the bar's midpoint within a zone of size l_m=1 mm, as shown by Fig. 12b (zone where d grows from 0 to 1). The plastic strain localizes around the fracture according to the profiles plotted in Fig. 12cd, and its growth obeys to two different evolution regimes: a regime of hardening plasticity for $p < \hat{p} = 1.4 \cdot 10^{-3}$, which produces an ascending response branch ($0.13 \cdot 10^{-3} < \varepsilon < 1.00 \cdot 10^{-3}$), and a regime of softening plasticity for $p > \hat{p}$, which corresponds to the softening branch of the response curve ($\varepsilon > 1.00 \cdot 10^{-3}$).

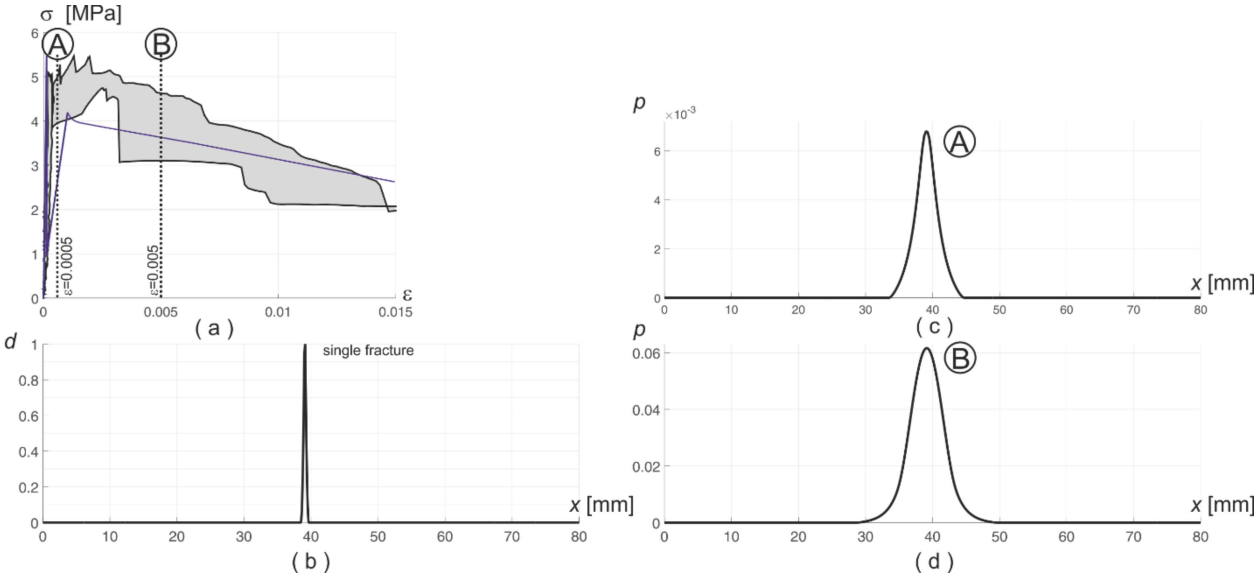

Figure 12. 1D tensile tests for 1.25% Vol. of fibers. Profiles of fracture field d (b), and plastic field p (c,d) at two different instants of the loading process.

Ductile failure. Samples with 2.55% Vol. of fibers experiences multi-cracking, as shown by Fig. 13, where profiles of d and p are drawn for different values of ε. The sequence of plots labeled by letters A, B, C and D show the progressive opening of cracks, always accompanied by stress drops in the σ-ε curve. As in the previous simulation, the first fracture forms near the bar midpoint (picture A), and, at the end of the multi-cracking stage, nine fractures have formed, spaced about 10 mm. The internal length l_b=15 mm provides an overestimate.

Pictures on the right column of Fig. 13 represents the profiles of p. The plastic strain attains maximum values at the crack points, where only the reinforcement can bear the tensile load, bridging it between the crack lips.

Plastic strain profiles B and C show that peak values are all equal except for one, that attains a smaller value. Indeed, if we analyze the plastic strain evolution in the interval between two consecutive fracture openings, we notice that the plastic strain at the new formed crack attains a peak value which is smaller than those at preexisting cracks. Then it grows, and, when the value of the preexisting peaks is reached, plastic strains increase in the whole bar. These two plastic strain evolution regimes correspond to the two different slopes of the response curve that can be noticed in some curve parts included between consecutive stress drops.

Picture E refers to the softening stage of macro-crack development in which plastic strains localizes around a single crack, and it grows in a region of size l_r=10 mm.

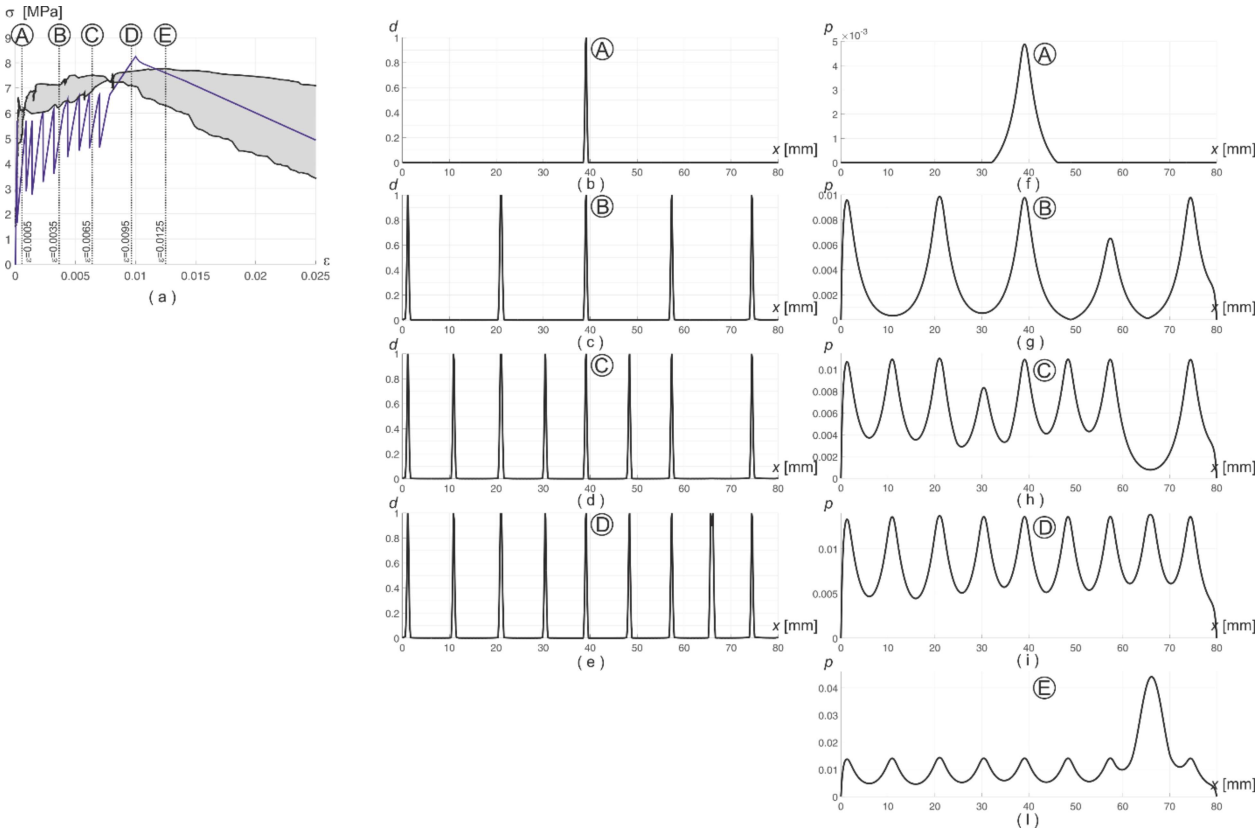

Figure 13. 1D tensile tests for 2.55% Vol. of fibers. Profiles of fracture field d (b,c,d,e), and plastic field p (f,g,h,i,l) at two different instants of the loading process.

5.2 2D tensile tests

In this section, beside discussing the evolution of d and p predicted by 2D simulations, we compare the numerical strain field at different values of ε with the strain contour plots of experiments, obtained from DIC. As described below, a close correspondence between simulations and experiments has been found, although the computational domain covers a small portion of the sample area.

Quasi-brittle failure. In case of 1.25% Vol. of fibers, a single fracture leads to the sample failure, as in the 1D case. Comparison of experimental and numerical longitudinal strain ε_y is proposed in Fig. 14. The simulation predicts the opening of a crack at an extremity of the thinner central part of the sample. Also in experiments, samples mainly fracture at the end of the fillets, because the inhomogeneous stress flux makes those zones more vulnerable. Snapshots labelled by letter B show that the thickness of the strain localization band predicted by the simulation matches that detected by DIC in experiments.

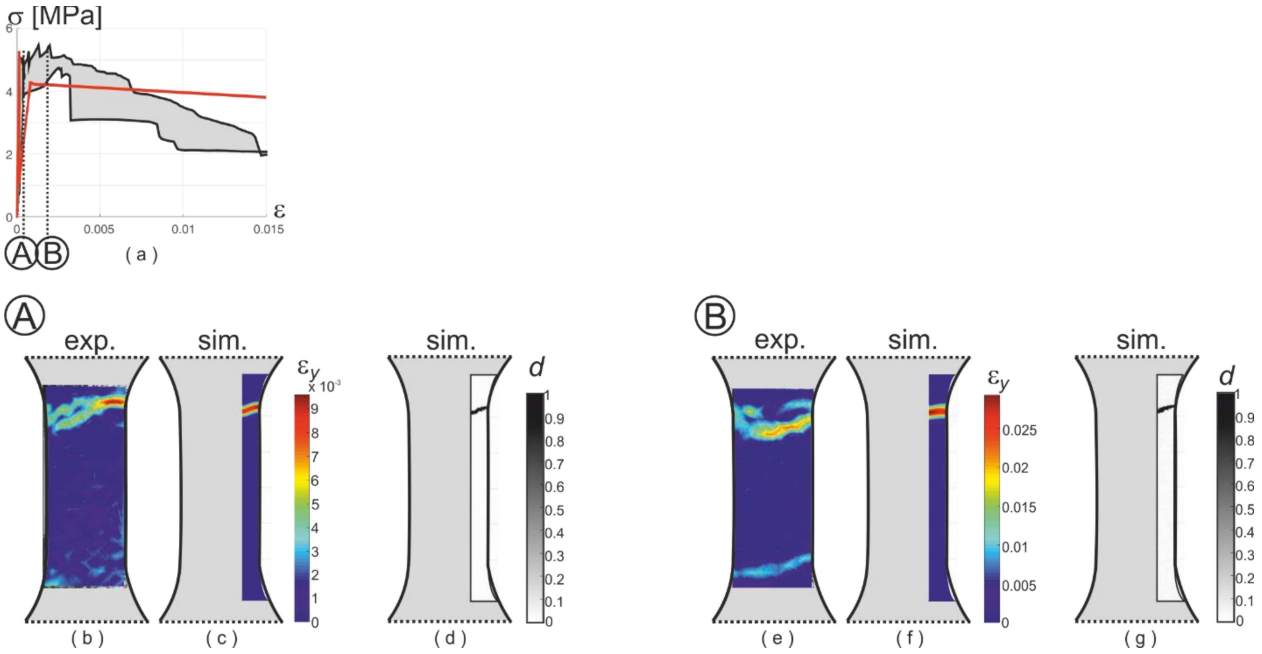

Figure 14. 2D tensile tests for 1.25% Vol. of fibers. Comparison of longitudinal strains ε_y measured in experiments by DIC, and resulting from numerical simulations at different deformations ε, and damage field d from simulations.

Ductile failure. Experimental and numerical snapshots of strain patterning are compared in Fig. 15, for samples with 2.55% Vol. of fibers. Damage field maps are also plotted in Fig. 15. Even in this case, the first crack opens at the extremity of the reduced-section zone (A), and, in the next steps of the evolution processes, further fractures open throughout the sample (B and C). We notice that cracks homogeneously distribute through the sample, and, going on with the tensile process, they increase in number, and reduce the inter-spacing. This process is closely predicted by the simulation. Indeed, the numerical strain maps B and C accurately match the experimental ones in terms of cracks number, inter-spacing, width of the strain localization bands (about l_r=10 mm) and strain values.

Experimental results show an irregular and fragmented strain patterning, with many localization bands that do not pass through the whole cross-section. This irregularity cannot be predicted by simulations because the computational domain is too small and, as above pointed out, the many inhomogeneities of tensile tests are not considered by the numerical model.

Regarding the damage field, fracture band are often larger than l_m=1 mm, and this is also due to the mesh size, which is not too fine. However, this inaccuracy does not affect significantly the results as shown by the mesh sensitivity analysis reported in the Appendix.

Finally, pictures D depict the situation of macro-crack opening. In the experiment, the macro-fracture mainly opens outside the area covered by DIC analysis, as shown by the red line, and just a small crack portion is captured inside the DIC rectangular region. We notice that the numerical strain values attained in the macro-crack localization band (red zone) are very close to those measured in the small fractured region at the bottom left corner of the DIC area. They attain the maximum value of about ε_y=0.03.

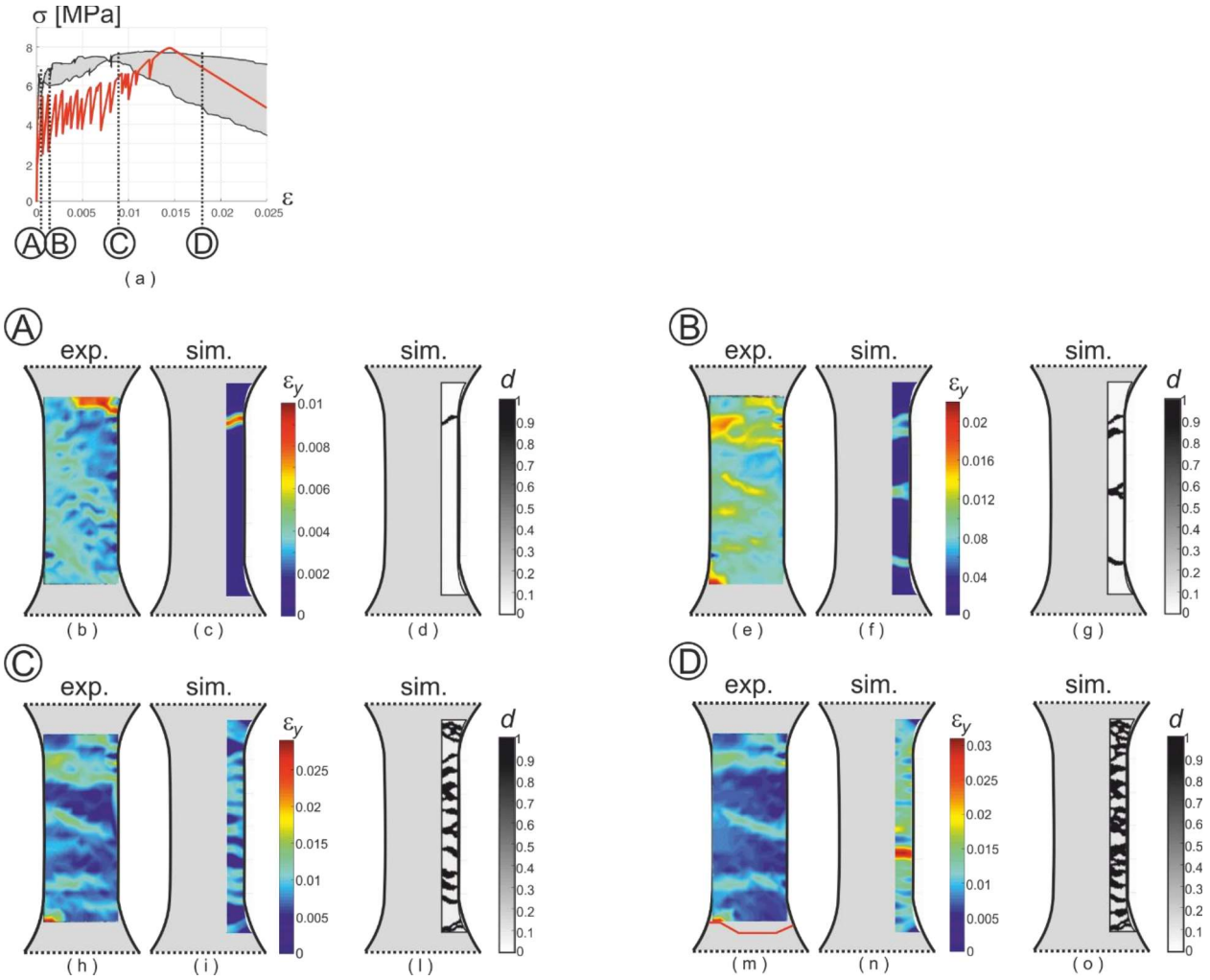

Figure 15. 2D tensile tests for 2.55% Vol. of fibers. Comparison of longitudinal strains ε_y measured in experiments by DIC, and resulting from numerical simulations at different deformations ε, and damage field d from simulations.

6. Conclusions

In this study, the uniaxial tensile behavior of soft cast UHPFRC has been investigated by varying the amount of hooked steel fibers, up to 2.55% by volume. Direct tensile tests have been carried out on dog-bone shaped specimens, with total length of 330 mm and cross-sectional area of about 45x30 mm^2. The full displacement field during tensile tests on UHPFRC specimens was obtained using DIC technology. Strain maps recorded on the specimen surface were useful to evaluate the damage evolution during the test and to compare experimental results with numerical simulations. Experiments showed that the addition of hooked steel fibers significantly modified the uniaxial tensile behavior of UHPFRC specimens, by avoiding brutal failure even at low fiber dosage (0.6% by volume). By varying the amount of steel fibers, two main different failure processes, *quasi-brittle* and *ductile*, have been identified. For low fiber dosage (≤1.25% Vol.), the initial elastic stretching is followed by a strain-softening phase in which a single crack progressively opens. For high fiber dosage (≥1.9% Vol.), a strain-hardening phase, characterized by multi- micro-cracking in the matrix, anticipates the softening process of single crack opening.

Then, a novel variational model has been proposed to better investigate the evolution of these different failure modes by solving an incremental energy minimization problem. The model

allowed to capture the main features of the mechanical behavior and the failure process experienced in UHPFRC by varying the amount of steel fibers. In particular, the model was able to identify the shift from 'strain-softening' to 'strain-hardening' behavior during the post-elastic stage, when a critical fibers volume threshold is exceeded.
Furthermore, the variational model developed in this study can be easily adapted to many other fiber-reinforced cementitious composites, to reproduce their mechanical behavior, by only changing the constitutive parameters values.

Appendix.

Mesh size sensitivity is investigated by considering two different meshes: a fine mesh of size 0.3 mm and a rough mesh of size 1.5 mm (see Fig. 16). Tensile tests are performed, and their results are reported in Figs. 17 and 18. The response curves of Fig. 17 differ only for the saw-tooth branches of multiple cracks opening, but, globally, they are very similar, capturing almost the same peak stress and corresponding strain. The multi-cracking branch associated to the rough mesh exhibits more pronounced stress-drops, because the damaged zones are broader than those obtained with fine mesh. Pictures of damage and plastic strain of Fig. 18 show that the mesh size does not significantly affect the evolution process. Indeed, in the two cases, cracks open according to the same sequence, and they form at equal positions. Differences just regard the size of the crack bands. Concerning the plastic strain, bands practically maintain the same size in the two simulations. Summing up, the use of a rough mesh leads to an inaccurate description of micro-fracture pattering, but it does not significantly affect the prediction of the whole tensile evolution process.

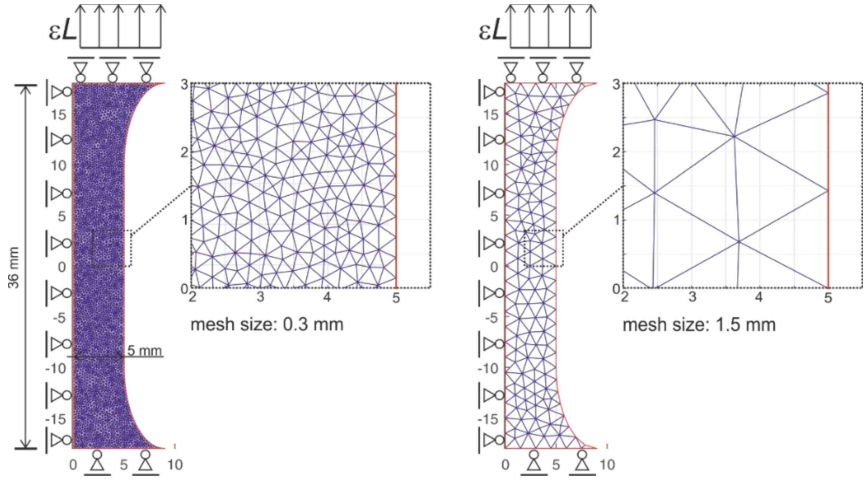

Figure 16. Domain discretized through fine and rough meshes. Meshes size are 0.3 mm and 1.5 mm.

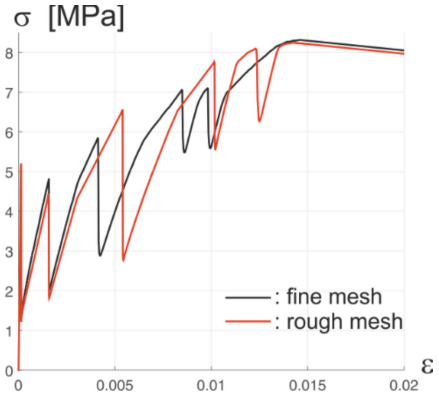

Figure 17. Stress-strain curves resulting from simulations performed with fine (black line) and rough (red line) meshes.

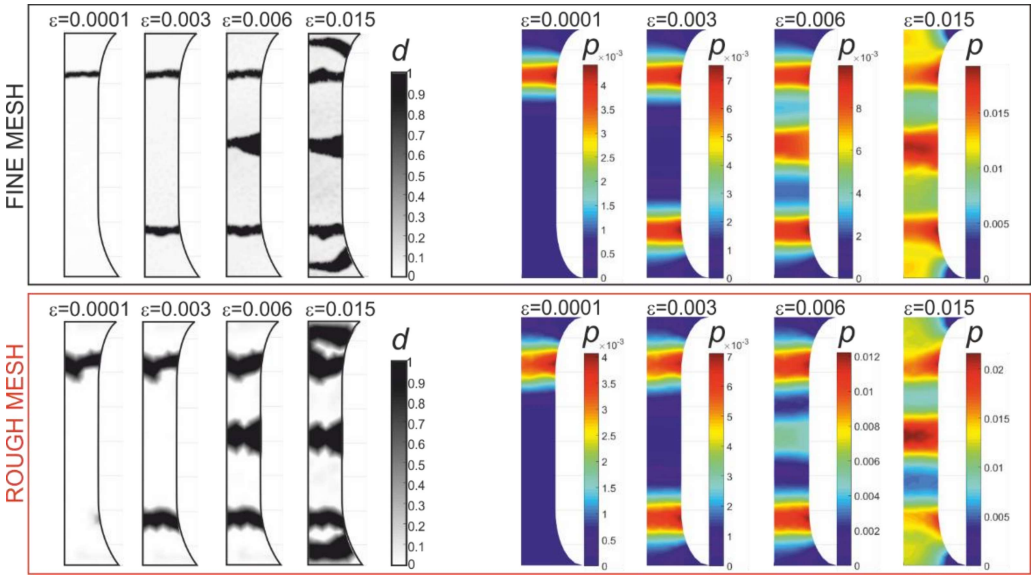

Figure 18. Snapshots of damage d, and cumulated plastic strain p at different deformation values in cases of fine and rough meshes.

Acknowledgments

G. Lancioni wish to acknowledge the financial support of PRIN funded Program "XFAST-SIMS: Extra fast and accurate simulation of complex structural systems". The authors gratefully acknowledge the useful help provided by the MD student Nicola Generosi in performing mechanical tests.

References

[1] AFGC / SETRA WORKING GROUP. Ultra High Performance Fibre-Reinforced Concrete – Interim Recommendations. Report, Assoc Française Génie Civil, Paris, Fr 2002.

[2] Japan Society of Civil Engineers. Recommendations for Design and Construction of High Performance Fiber Reinforced Cement Composites with Multiple Fine Cracks (HPFRCC). Concr Eng Ser 2008.

[3] Shen X, Brühwiler E. Influence of local fiber distribution on tensile behavior of strain hardening UHPFRC using NDT and DIC. Cem Concr Res 2020. doi:10.1016/j.cemconres.2020.106042.

[4] Yu J, Zhang B, Chen W, He J. Experimental and multi-scale numerical investigation of ultra-high performance fiber reinforced concrete (UHPFRC) with different coarse aggregate content and fiber volume fraction. Constr Build Mater 2020. doi:10.1016/j.conbuildmat.2020.120444.
[5] Maya Duque LF, Graybeal B. Fiber orientation distribution and tensile mechanical response in UHPFRC. Mater Struct Constr 2017. doi:10.1617/s11527-016-0914-5.
[6] Azmee NM, Shafiq N. Ultra-high performance concrete: From fundamental to applications. Case Stud Constr Mater 2018. doi:10.1016/j.cscm.2018.e00197.
[7] Al-Osta MA, Isa MN, Baluch MH, Rahman MK. Flexural behavior of reinforced concrete beams strengthened with ultra-high performance fiber reinforced concrete. Constr Build Mater 2017. doi:10.1016/j.conbuildmat.2016.12.094.
[8] Yoo DY, Banthia N. Mechanical and structural behaviors of ultra-high-performance fiber-reinforced concrete subjected to impact and blast. Constr Build Mater 2017. doi:10.1016/j.conbuildmat.2017.05.136.
[9] Habert G, Denarié E, Šajna A, Rossi P. Lowering the global warming impact of bridge rehabilitations by using Ultra High Performance Fibre Reinforced Concretes. Cem Concr Compos 2013. doi:10.1016/j.cemconcomp.2012.11.008.
[10] Naaman AE. High Performance Fiber Reinforced Cement Composites: Classification and Applications. CBM-CI Int Work Karachi, Pakistan 2009. doi:978-969-8620-06-6.
[11] Corinaldesi V, Donnini J, Nardinocchi A. The influence of calcium oxide addition on properties of fiber reinforced cement-based composites. J Build Eng 2015;4. doi:10.1016/j.jobe.2015.07.009.
[12] Wang D, Shi C, Wu Z, Xiao J, Huang Z, Fang Z. A review on ultra high performance concrete: Part II. Hydration, microstructure and properties. Constr Build Mater 2015. doi:10.1016/j.conbuildmat.2015.08.095.
[13] Yoo DY, Banthia N. Mechanical properties of ultra-high-performance fiber-reinforced concrete: A review. Cem Concr Compos 2016. doi:10.1016/j.cemconcomp.2016.08.001.
[14] Richard P, Cheyrezy M. Composition of reactive powder concretes. Cem Concr Res 1995. doi:10.1016/0008-8846(95)00144-2.
[15] Yu R, Spiesz P, Brouwers HJH. Mix design and properties assessment of Ultra-High Performance Fibre Reinforced Concrete (UHPFRC). Cem Concr Res 2014. doi:10.1016/j.cemconres.2013.11.002.
[16] Hassan AMT, Jones SW, Mahmud GH. Experimental test methods to determine the uniaxial tensile and compressive behaviour of Ultra High Performance Fibre Reinforced Concrete(UHPFRC). Constr Build Mater 2012. doi:10.1016/j.conbuildmat.2012.04.030.
[17] Corinaldesi V, Nardinocchi A, Donnini J. The influence of expansive agent on the performance of fibre reinforced cement-based composites. Constr Build Mater 2015;91. doi:10.1016/j.conbuildmat.2015.05.002.
[18] Jones T, Cather B. Ultra-high performance fibre-reinforced concrete. Concr Eng Int 2005.
[19] Naaman AE, Reinhardt HW. Proposed classification of HPFRC composites based on their tensile response. Mater Struct Constr 2006. doi:10.1617/s11527-006-9103-2.
[20] Wille K, Kim DJ, Naaman AE. Strain-hardening UHP-FRC with low fiber contents. Mater Struct Constr 2011. doi:10.1617/s11527-010-9650-4.
[21] Wille K, El-Tawil S, Naaman AE. Properties of strain hardening ultra high performance fiber reinforced concrete (UHP-FRC) under direct tensile loading. Cem Concr Compos 2014. doi:10.1016/j.cemconcomp.2013.12.015.
[22] FIB. Model Code 2010. Fib Model Code Concr Struct 2010 2011. doi:10.1002/9783433604090.ch6.
[23] Consiglio Superiore dei Lavori Pubblici – Servizio Tecnico Centrale. Linea guida per

l'identificazione, la qualificazione, la certificazione di valutazione tecnica ed il controllo di accettazione dei calcestruzzi fibrorinforzati FRC (Fiber Reinforced Concrete) n.d.
[24] Consiglio Nazionale delle Ricerche (CNR). Istruzioni per la Progettazione, l'Esecuzione ed il Controllo di Strutture di Calcestruzzo Fibrorinforzato 2006.
[25] Kamal A, Kunieda M, Ueda N, Nakamura H. Evaluation of crack opening performance of a repair material with strain hardening behavior. Cem Concr Compos 2008. doi:10.1016/j.cemconcomp.2008.08.003.
[26] Jun P, Mechtcherine V. Behaviour of strain-hardening cement-based composites (SHCC) under monotonic and cyclic tensile loading: Part 1 - Experimental investigations. Cem Concr Compos 2010. doi:10.1016/j.cemconcomp.2010.07.019.
[27] Wille K, Naaman AE, El-Tawil S, Parra-Montesinos GJ. Ultra-high performance concrete and fiber reinforced concrete: Achieving strength and ductility without heat curing. Mater Struct Constr 2012. doi:10.1617/s11527-011-9767-0.
[28] Naaman AE, Homrich JR. Tensile stress-strain properties of SIFCON. ACI Mater J 1989.
[29] Malárics V, Müller HS. Evaluation of the splitting tension test for concrete from a fracture mechanical point of view the. Proc Fract Mech Concr Concr Struct - Assessment, Durability, Monit Retrofit Concr Struct 2010.
[30] Li Z, Kulkarni SM, Shah SP. New test method for obtaining softening response of unnotched concrete specimen under uniaxial tension. Exp Mech 1993. doi:10.1007/BF02322570.
[31] Yoo DY, Kim S, Kim JJ, Chun B. An experimental study on pullout and tensile behavior of ultra-high-performance concrete reinforced with various steel fibers. Constr Build Mater 2019. doi:10.1016/j.conbuildmat.2019.02.058.
[32] Richard P, Cheyrezy MH. Reactive powder concretes with high ductility and 200-800 Mpa compressive strength. Proc. V. Mohan Malhotra Symp., 1994. doi:10.14359/4536.
[33] Lancioni G, Alessi R. Modeling micro-cracking and failure in short fiber-reinforced composites. J Mech Phys Solids 2020;137:103854. doi:10.1016/j.jmps.2019.103854.
[34] Marigo JJ, Maurini C, Pham K. An overview of the modelling of fracture by gradient damage models. Meccanica 2016. doi:10.1007/s11012-016-0538-4.
[35] Piero G Del, Lancioni G, March R. A diffuse cohesive energy approach to fracture and plasticity: The one-dimensional case. J Mech Mater Struct 2013. doi:10.2140/jomms.2013.8.109.
[36] Lancioni G. Modeling the Response of Tensile Steel Bars by Means of Incremental Energy Minimization. J Elast 2015. doi:10.1007/s10659-015-9515-8.
[37] Lancioni G, Yalçinkaya T, Cocks A. Energy-based non-local plasticity models for deformation patterning, localization and fracture. Proc R Soc A Math Phys Eng Sci 2015. doi:10.1098/rspa.2015.0275.
[38] Jirásek M, Rolshoven S. Localization properties of strain-softening gradient plasticity models. Part II: Theories with gradients of internal variables. Int J Solids Struct 2009. doi:10.1016/j.ijsolstr.2008.12.018.
[39] Alessi R, Marigo JJ, Vidoli S. Gradient damage models coupled with plasticity: Variational formulation and main properties. Mech Mater 2015. doi:10.1016/j.mechmat.2013.12.005.
[40] Alessi R, Marigo JJ, Maurini C, Vidoli S. Coupling damage and plasticity for a phase-field regularisation of brittle, cohesive and ductile fracture: One-dimensional examples. Int J Mech Sci 2018. doi:10.1016/j.ijmecsci.2017.05.047.
[41] Lancioni G, Corinaldesi V. Variational modelling of diffused and localized damage with applications to fiber-reinforced concretes. Meccanica 2018. doi:10.1007/s11012-017-0709-y.
[42] BS-EN197-1: Cement Part 1: Composition, Specifications and Conformity Criteria for

Common Cements. Br Stand 2011.
[43] BSI EN 1015-11. Methods of Test for Mortar for Masonry: Part 11: Determination of Flexural and Compressive Strength of Hardened Mortar. Bs En 1015 2006.
[44] Yoo DY, Banthia N, Kang ST, Yoon YS. Effect of fiber orientation on the rate-dependent flexural behavior of ultra-high-performance fiber-reinforced concrete. Compos Struct 2016. doi:10.1016/j.compstruct.2016.08.023.
[45] Song Q, Yu R, Shui Z, Wang X, Rao S, Lin Z. Optimization of fibre orientation and distribution for a sustainable Ultra-High Performance Fibre Reinforced Concrete (UHPFRC): Experiments and mechanism analysis. Constr Build Mater 2018. doi:10.1016/j.conbuildmat.2018.02.130.
[46] Amodio D, Broggiato GB, Campana F, Newaz GM. Digital speckle correlation for strain measurement by image analysis. Exp Mech 2003. doi:10.1177/0014485103434004.
[47] Sutton MA, Yan JH, Tiwari V, Schreier HW, Orteu JJ. The effect of out-of-plane motion on 2D and 3D digital image correlation measurements. Opt Lasers Eng 2008. doi:10.1016/j.optlaseng.2008.05.005.
[48] Badaloni M, Rossi M, Chiappini G, Lava P, Debruyne D. Impact of Experimental Uncertainties on the Identification of Mechanical Material Properties using DIC. Exp Mech 2015. doi:10.1007/s11340-015-0039-8.
[49] Mielke, A., Roubícek T. Rate-Independent Systems: Theory and Application. Springer 2015.
[50] Pham K, Amor H, Marigo JJ, Maurini C. Gradient damage models and their use to approximate brittle fracture. Int. J. Damage Mech., 2011. doi:10.1177/1056789510386852.
[51] Ambrosio L, Tortorelli VM. Approximation of functional depending on jumps by elliptic functional via t- convergence. Commun Pure Appl Math 1990. doi:10.1002/cpa.3160430805.
[52] Ambrosio, L., Tortorelli VM. On the approximation of free discontinuity problems. Boll Un Mat Ital 1992;6-B:105–123.
[53] Aifantis EC. The physics of plastic deformation. Int J Plast 1987. doi:10.1016/0749-6419(87)90021-0.
[54] Mühlhaus HB, Alfantis EC. A variational principle for gradient plasticity. Int J Solids Struct 1991. doi:10.1016/0020-7683(91)90004-Y.
[55] Gurtin ME, Anand L. Thermodynamics applied to gradient theories involving the accumulated plastic strain: The theories of Aifantis and Fleck and Hutchinson and their generalization. J Mech Phys Solids 2009. doi:10.1016/j.jmps.2008.12.002.
[56] Gurtin ME, Fried E, Anand L. The Mechanics and Thermodynamics of Continua. 2010. doi:10.1017/cbo9780511762956.
[57] Lancioni G, Royer-Carfagni G. The variational approach to fracture mechanics. a practical application to the french panthéon in Paris. J Elast 2009. doi:10.1007/s10659-009-9189-1.